ASSESSING RENEWABLE RESOURCE PENETRATION ON POWER SYSTEM SMALL-SIGNAL REACHABILITY

BY

YU CHEN

THESIS

Submitted in partial fulfillment of the requirements
for the degree of Master of Science in Electrical and Computer Engineering
in the Graduate College of the
University of Illinois at Urbana-Champaign, 2011

Urbana, Illinois

Adviser:

Assistant Professor Alejandro D. Domínguez-García

ABSTRACT

This thesis proposes a method to assess the impact on power system dynamic performance caused by uncertainty in the system supply side. Operational uncertainty, e.g., demand variability, is not new to power systems. However, with the increased penetration of renewable-based generation, operational uncertainty will extend to a significant portion of the supply side, which may have an impact on system dynamic performance, e.g., frequency or voltage deviations beyond prescribed operational requirements. To address the problem, we propose the use of reachability analysis techniques, which provide bounds on worst-case deviations of system variables that must remain within certain operational constraints. We assume the input disturbance caused by the renewable-based generation is small enough to justify linearization of the power system around a nominal trajectory. If the reach set is within the region defined by system operational requirements, then we conclude the disturbance caused by the renewable resource does not have a significant impact on system dynamic performance. The method is illustrated with several case studies. In particular, we show the method successfully provides reachability results for a sizable benchmark system that contains 140 buses and 48 synchronous machines, which accounts for a total of 294 dynamic states.

To my parents, Abby and Jie

ACKNOWLEDGMENTS

I would like to thank Professor Alejandro Domínguez-García for his guidance, support, and patience over the past two years, without which this work would not have been possible. Always eager to share his insight and ideas, Alejandro has been a true collaborator and mentor. I also owe thanks to Professor Peter W. Sauer for his invaluable suggestions throughout this project.

TABLE OF CONTENTS

LIST OF TABLES vii

LIST OF FIGURES viii

CHAPTER 1 INTRODUCTION 1
1.1 Background 1
1.2 Statement of Problem 2
1.3 Related Work 3
1.4 Contribution of Thesis 4

CHAPTER 2 MODEL 7
2.1 System Description 7
2.2 Nominal Trajectory 9
2.3 Nonlinear Ordinary Differential Equation Model 10
2.4 Bounding the Disturbance Input 12
2.5 Linearized Model 14

CHAPTER 3 REACH SET CALCULATION 16
3.1 Linearized Model Reach Set Calculation 16
3.2 Choice of Free Parameter, $\beta(t)$ 17
3.3 Dynamic Performance Requirements 24
3.4 Note on Small-Signal Approximation 25

CHAPTER 4 APPLICATION OF REACHABILITY ANALYSIS TO POWER SYSTEMS 27
4.1 Renewable-Based Power Injection 27
4.2 Unknown-but-Bounded Model 29
4.3 Linearized Power System Model 30
4.4 Comparison Between Two Renewable-Based Power Injection Models 32
4.5 Reach Set Computation 33
4.6 Reach Set Visualization 33

CHAPTER 5 THREE-BUS SYSTEM WITH CONVENTIONAL AND RENEWABLE-BASED POWER GENERATION 34
5.1 Small-Signal Model 35
5.2 Reachability Numerical Analysis 37

CHAPTER 6 CASE STUDIES 38
6.1 WECC 3-Machine Test Case 38
6.2 New England 10-Machine Test Case 40
6.3 NPCC 48-Machine Test Case 47
6.4 Summary 51

CHAPTER 7 CONCLUSIONS 52

APPENDIX A CONTINUOUS-TIME UNKNOWN-BUT-BOUNDED PROCESS 56
A.1 Definitions 56
A.2 Derivation of Ellipsoidal Equation 57

APPENDIX B PROJECTIONS OF SETS 61

APPENDIX C MATLAB IMPLEMENTATION DETAILS 62
C.1 System Matrices from PST 62
C.2 Conversion from Per-Unit Speed 63
C.3 Removal of Zero-Eigenvalue Associated with Reference Angle . 63
C.4 Application of Singular Perturbation Model 64
C.5 Augmentation of Renewable Resource Dynamics 65
C.6 Solution of Reachability Problem 66

REFERENCES 67

LIST OF TABLES

2.1 SMIB system model parameter values 9

5.1 Three-Bus System Model Parameter Values 37

6.1 Machines Replaced with Renewable Resources in New England System Test Cases 40

LIST OF FIGURES

2.1 Brief description of system model. 7
2.2 Single-machine infinite-bus system. 8
2.3 Uncertainty in $v_\infty(t)$ for SMIB examples. 10
2.4 $\mathcal{W}$ is bounded by Ω_w. 13

3.1 Single-machine infinite-bus system reachability analysis results for 10% input uncertainty. 18
3.2 The eigenvalues of A, denoted by λ, are all in the open left half complex plane. The maximum value that β_0 can take and still maintain the stability of $\Psi_{\beta_0}(t)$, denoted by βmax, is shown. 23
3.3 Single-machine infinite-bus large-signal worst-case trajectory and linearized model reach set for 20% input uncertainty. 25

4.1 Model of general process that governs renewable resource i. . . 27
4.2 Renewable-based power injection model for power injection at node i. 30
4.3 Renewable-based power injection model for power injection at nodes i and j. 32

5.1 Three-bus system with renewable-based power injection. . . . 34
5.2 Three-bus system reachability analysis results 37

6.1 Simplified WECC linearized model with uncertainty in P_w. . . 39
6.2 New England test case - 20% renewable penetration: reachability results for $\Delta\omega_5$ vs. $\Delta\delta_5$, ± 0.2 input uncertainty 42
6.3 New England test case - 20% renewable penetration: reachability results for $\Delta\omega_3$ vs. $\Delta\delta_3$, ± 0.2 input uncertainty 43
6.4 New England test case - 20% renewable penetration: reachability results for $\Delta\omega_5$ vs. $\Delta\omega_3$, ± 0.1 input uncertainty 43
6.5 New England test case - 20% renewable penetration: reachability results for $\Delta\omega_5$ vs. $\Delta\delta_5$, unknown-but-bounded small-signal wind speeds 44

6.6 New England test case - 20% renewable penetration: reachability results for $\Delta\omega_7$ vs. $\Delta\omega_2$, ± 2 m/s uncertainty in wind speed 45
6.7 New England test case - 30% renewable penetration A: reachability results for $\Delta\omega_5$ vs. $\Delta\delta_5$, unknown-but-bounded small-signal wind speeds 46
6.8 New England test case - 30% renewable penetration B: reachability results for $\Delta\omega_5$ vs. $\Delta\delta_5$, unknown-but-bounded small-signal wind speeds 46
6.9 NPCC test case - 10% renewable penetration A: reachability results for $\Delta\omega_{12}$ vs. $\Delta\delta_{12}$, unknown-but-bounded small-signal wind speeds 48
6.10 NPCC test case - 10% renewable penetration comparison between two machine configurations: reachability results for $\Delta\omega_{12}$ vs. $\Delta\delta_{12}$, wind speed uncertainty of ± 2 m/s 48
6.11 NPCC test case - 20% renewable penetration A: reachability results for $\Delta\omega_{12}$ vs. $\Delta\delta_{12}$, unknown-but-bounded small-signal wind speeds 50
6.12 NPCC test case - 20% renewable penetration comparison between two machine configurations: reachability results for $\Delta\omega_{12}$ vs. $\Delta\delta_{12}$, wind speed uncertainty of ± 2 m/s 50
6.13 NPCC test case - 20% renewable penetration: reachability results for $\Delta\omega_{41}$ vs. $\Delta\omega_8$, ± 2 m/s wind speed uncertainty . . . 51

CHAPTER 1

INTRODUCTION

The motivation for this work lies in the current trend toward more environmentally friendly and responsible electricity production in the electrical power sector. The push for energy independence requires increased penetration of renewable resources of electricity, such as wind and solar generation, into the power grid. In this introductory chapter, we outline the necessity for developing a tool to assess the impact of increased penetration of renewable resources on power system dynamic performance, review related research to put this thesis in context, and finish with the main contributions of this thesis.

1.1 Background

The integration of renewable resources into the power grid presents notable challenges to the operations and planning of today's power systems [1] because these resources are

- highly variable, e.g., wind generation is much higher during the nighttime than daytime;
- highly intermittent, e.g., solar generation can vary greatly between cloudy and sunny conditions;
- uncontrollable, e.g., cloud movements, which can cause partial shading on solar panels, cannot be controlled so as to yield the desired power output level; and
- uncertain — renewable power generation is difficult to forecast since it often depends on weather conditions (e.g., wind and solar).

The lack of accurate forecasts causes renewable power generation to become uncertain contributions to existing power systems. In actuality, uncertainty is not new to power systems. Examples include the system load, availability of generators and other system facilities, maintenance of transmission lines, etc. [2]. Since there must be a balance between generation and load at all times, the generation must follow the load. Power system operators compensate for load uncertainty by allocating spinning reserves. In fact, demand-side uncertainty is likely to increase, due to the addition of demand response programs. Together, these represent major additional sources of uncertainty with respect to managing power systems.

Faced with these uncertainties, power system operators — typically independent system operators (ISOs) — must compensate with additional insurance for their system through increased level of reserves to satisfy steady-state power balance [3]. Deep levels of renewable resource penetration in the system can also impact system dynamic performance, i.e., small-signal and transient stability, due to reduced effective inertia of the system [4]. Small-signal stability is concerned with the ability of the power system to maintain synchronism under disturbances that are sufficiently small that linearization of system equations is adequate for analysis. Transient stability is concerned with the ability of the power system to maintain synchronism when subjected to a severe disturbance [5]. The time frame of interest in these stability studies is on the order of 10 to 20 seconds following a disturbance [5].

1.2 Statement of Problem

As the presence of renewable-based generation in the power grid increases, new tools are necessary to assess their impact on the security of supply and load balancing in near real-time. This thesis focuses on a particular aspect of the impact of renewable resource penetration on system dynamic performance. We address how system variables may deviate from steady-state operating points due to the uncertainties in the power system, in particular those introduced by penetration of renewable resources. We provide a method to assess whether certain variables remain within acceptable ranges while the system is subject to uncontrolled disturbances caused by uncertainty in renewable-based generation.

1.3 Related Work

The reachability problem in the context of power systems in the presence of uncertainty has been explored in the past. In general, the existing works tend to differ in the way in which uncertainty is captured in power system computation. They can be loosely divided into two categories: uncertainty in the context of static performance and in the context of dynamic performance.

1.3.1 Static Performance of Power Systems

Various approaches to address uncertainty in power systems have been explored before in the context of static power flow analysis. For example, [6] described three ways of capturing uncertainty in power flow computation: probabilistic methods, interval mathematics, and fuzzy arithmetic techniques. Of particular interest is the interval method, which uses the notion of an interval — a set of numbers on the real axis, characterized by its two extreme values. A vector interval is a vector where every element is an interval variable. This method was utilized to solve the power flow reachability problem in [7], and results were compared with those obtained from stochastic and Monte Carlo methods. The conclusions were somewhat pessimistic regarding the general applicability of interval methods to large-scale systems.

The effect of model uncertainty on transmission security in a power market was explored in [8]. Two types of uncertainty were considered: structural, which were modelled by contingency scenarios, and perturbation of model parameters, which were quantified by sensitivity analysis. The authors used a linearized power flow model to study the benchmark example of the New England/New York interconnection. Interval analysis, which was presented in [6], was applied to the optimization of electric energy markets in [9]. Again, a linearized power system model was utilized to explore the worst-case effects of network parameter uncertainties modelled with the interval method on various optimization problems solved at the ISO level in a deregulated power market. Furthermore, Saric and Stankovic used ellipsoidal approximations in power system optimization to obtain ranges in which generator injections can vary without violating static operational constraints in security analysis [10]. The model was applied to the optimal economic dispatch problem and the calculation of locational marginal prices in a day-ahead market.

1.3.2 Dynamic Performance of Power Systems

Several approaches to addressing uncertainty in dynamic performance assessment in the context of power systems have been proposed in the past. For example, the probabilistic collocation method (PCM) is used to develop relationships between uncertain parameters and outputs of interest in [11]. PCM creates polynomial models relating the uncertain parameters of the system to the outputs of interest. It was applied to a portion of a dynamic model which describes a large portion of the western United States and demonstrated significant time savings as compared to traditional Monte Carlo analysis. This technique is computationally efficient when the number of uncertain parameters is relatively small.

Other approaches have been proposed to address uncertainty in dynamic performance assessment. For example, [12] has shown that trajectory sensitivities can be used to generate accurate first-order approximations of trajectories that arise from perturbed parameter sets. Hiskens and Alseddiqui proposed to linearize the system around a nominal trajectory, as compared to small disturbance analysis, the analysis for which is performed on linearizations around an equilibrium point. For the worst-case analysis, [12] utilized orthotopes to represent the uncertain parameter set. A similar technique is presented in [13] for application to differential-algebraic-discrete models, which are common to hybrid systems.

Regarding reachability in power systems, Jin et al. used backward reachable sets to compute the stability region of an equilibrium point [14]. The methodology was applied to the classical single-machine infinite-bus system. The authors concluded that the method suffers from the "curse of dimensionality"; therefore, the methodology would be difficult to scale to larger systems.

1.4 Contribution of Thesis

Consideration for uncertainty in dynamic performance assessment is computationally challenging. Statistical and worst-case characterizations are complementary in the analysis of risk involved with power system operations. We study the worst-case approach, as this provides power system operators with a guarantee of system security as opposed to a probabilistic figure that

ensures the system will be secure over the desired time frame.

In this thesis, we provide an analytically tractable method, which is also amenable for computer implementation, to assess whether certain variables of interest, such as the system frequency and bus voltages, remain within acceptable ranges while the system is subject to uncontrolled disturbances caused by the uncertainties in renewable resources (the result of forecast error). The results presented in [15] indicate that a negative load model suffices to represent type-C wind power generators, which are based on doubly-fed induction generators. Hence, we assume that power system dynamics are described by the nonlinear differential-algebraic equation (DAE) formulation [16], where the effect of the renewable power injection is modelled as an uncontrolled disturbance to the system dynamics. In this setup, the problem can be addressed by computing the reach set or attainability domain [17], i.e., the set that bounds all possible system trajectories that arise from all possible renewable resource power injection scenarios.

We model uncertain inputs, such as power injection from renewable resources, as unknown quantities constrained between minimum and maximum values, similar to vector intervals in [6]. We subsequently compute the reach set of the power system using ellipsoidal approximations of the input set. The advantages of using ellipsoids include their explicit form of approximation, smoothness of the boundaries of the approximating sets, possibility of optimization, etc. [18]. Computing the exact reach set may be very difficult, or even impossible, especially for nonlinear DAEs. Therefore, we assume the disturbances introduced by renewable resources are sufficiently small as to justify the use of a small-signal approximation. Similar to the procedure described in [12] and [13], the DAE is linearized around some nominal trajectory instead of an equilibrium point, where the nominal trajectory is determined by the resource forecast. In our model, the forecast errors provide bounds on the variability of renewable-based generation injected in the system. These bounds are used in conjunction with the linearized model to compute the reach set. If the reach set is within the region of the state-space defined by system operational requirements, e.g., maximum system frequency deviation, then we conclude the disturbance due to uncertainty in the renewable resource does not have a significant impact on system dynamic performance.

We begin by developing the linearized model from the nonlinear differential-algebraic equations that govern power systems in Chapter 2 as well as the

unknown-but-bounded input uncertainty model for renewable resources. In Chapter 3, we elaborate on the unknown-but-bounded input model and outline the method with which we obtain system reach sets. We connect reachability concepts back to the power system model in Chapter 4 and describe associated uncertainty models and subsequent reach set calculations. We apply the concepts in previous chapters to a small three-bus power system example in Chapter 5 and present analytical as well as simulation results. Next, large-scale power system test cases are described and their corresponding reachability results are presented in Chapter 6. Finally, concluding remarks are made in Chapter 7.

CHAPTER 2

MODEL

In this chapter, we derive a linearized model from the canonical nonlinear differential-algebraic equation (DAE) power system model. This linearized model will be later used in our studies. The general procedure is summarized in Fig. 2.1.

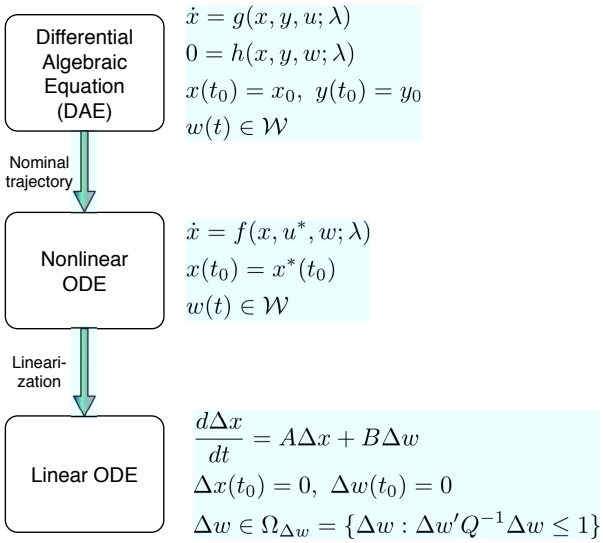

Figure 2.1: Brief description of system model.

2.1 System Description

Electric power systems can be described by a DAE model of the form

$$\dot{x} = g(x, y, u; \lambda), \tag{2.1}$$

$$0 = h(x, y, w; \lambda), \tag{2.2}$$

where $x \in \mathbb{R}^n$, $y \in \mathbb{R}^p$, $u \in \mathbb{R}^m$, $w \in \mathbb{R}^l$, and $\lambda \in \mathbb{R}^q$. Also, $f : \mathbb{R}^{n+p+m+q} \mapsto \mathbb{R}^n$ and $h : \mathbb{R}^{n+p+l+q} \mapsto \mathbb{R}^p$.

Here, x would include machine dynamic states, such as synchronous machine angles, speeds, and fluxes; $y \in \mathbb{R}^p$ would include network variables, such as load bus voltage magnitudes and angles; $u \in \mathbb{R}^m$ would include set points, such as the voltage regulator reference and steam valve position; $w \in \mathbb{R}^l$ would include uncontrolled disturbances, such as load demand changes or renewable-based power generation uncertainty; and λ could represent a diverse range of parameters, including loads and line impedances.

Initial conditions for the model in (2.1)-(2.2) are given by

$$x(t_0) = x_0, \tag{2.3}$$

$$y(t_0) = y_0, \tag{2.4}$$

$$u(t_0) = u_0, \tag{2.5}$$

$$w(t_0) = w_0, \tag{2.6}$$

where y_0 is a solution of $h(x_0, y_0, w_0; \lambda) = 0$. Since h is, in general, nonlinear, $h = 0$ may have several solutions for a given set of x_0, u_0, w_0, and λ. In the context of power systems, we can usually isolate the correct solution by applying some common sense rules to the algebraic power flow results.

Throughout this chapter, we illustrate our developments with a running example involving the canonical power system model — the single-machine infinite-bus (SMIB) system — as depicted in Fig. 2.2. The parameter values for this example are listed in Table 2.1, where all values are per-unit unless otherwise indicated.

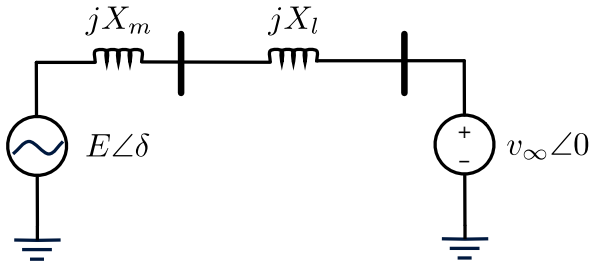

Figure 2.2: Single-machine infinite-bus system.

***Example* 1** (SMIB)**.** Let δ be the angular position of the rotor in electrical radians, and ω be the angular velocity of the rotor in electrical rad/s. Then,

Table 2.1: SMIB system model parameter values

E	X_m	X_l	M	D [s/rad]	P_m	ω_s [rad/s]
1	0.2	0.066	$\frac{1}{15\pi}$	0.04	1	120π

the system can be described by the following DAE:

$$\dot{\delta} = \omega - \omega_s, \tag{2.7}$$

$$\dot{\omega} = \frac{1}{M}\left[P_m - P_e - D(\omega - \omega_s)\right], \tag{2.8}$$

$$0 = P_e - \frac{Ev_\infty}{X_l + X_m}\sin\delta, \tag{2.9}$$

where, following the notation in (2.1)-(2.2), $\lambda = [E, X_m, X_l, M, D, \omega_s]'$ [16], $x = [\delta \quad \omega]'$, $y = P_e$, and $u = P_m$. In this case, since $v_\infty > 0$ models the external system to which the machine is connected, we assume that v_∞ is subject to uncertainty, and thus $w = v_\infty$. Here, (2.7) and (2.8) are the differential equations of the DAE model, while (2.9) is the algebraic power flow relation. $\lhd$

2.2 Nominal Trajectory

In this work, we assume the system (2.1)-(2.2) is operating with nominal inputs $u(t) = u^*(t)$ and the uncertain disturbance $w(t)$ (e.g., load demand, wind speed, and solar clearness index) is restricted to some margin around an operating point $w(t) = w^*(t)$, and $w(t)$ is bounded in some set $\mathcal{W}(t)$ (possibly time-varying) during the time horizon of interest $t \in [t_0, T]$. We envision our tool to be used in power systems operations, so $T - t_0$ is likely within the range of an hour, where uncertainties in the system can be captured relatively accurately. In this regard, $\mathcal{W}(t)$ can be interpreted as the forecast error of $w(t)$ for $t \in [t_0, T]$. We illustrate these ideas with our running example.

***Example* 2** (SMIB)**.** As discussed in Example 1, $u(t) = P_m(t)$ and $w(t) = v_\infty(t)$. To simplify the example, we assume the deterministic input to be a constant value in the time horizon of interest $t \in [t_0, T]$, i.e., $P_m^*(t) = P_m^*$. We also assume the nominal realization of the uncertain input is constant so that $v_\infty^*(t) = v_m$. In this example, we assume $v_\infty(t)$ is bounded within some

neighbourhood of v_m, more specifically,

$$v_\infty(t) \in \mathcal{W}_{v_\infty}(t) = \{v_\infty(t) : |v_\infty(t) - v_m| \leq k(t)v_m\}, \tag{2.10}$$

with $k(t) > 0$ and $v_m > 0$. In this series of examples involving the SMIB, we assume $v_m = 1$ p.u. While $k(t)$ may, in general, be time-varying, in this example we take $k = \max_{t\in[t_0,T]} k(t)$, a constant error bound on v_∞. This concept is illustrated in Fig. 2.3.

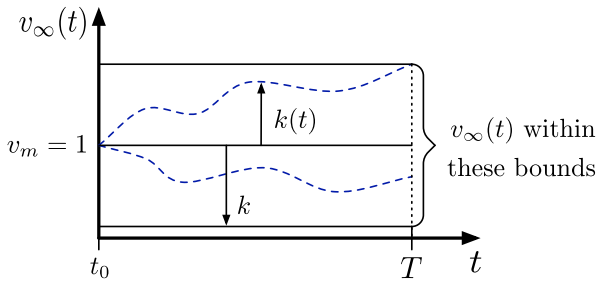

Figure 2.3: Uncertainty in $v_\infty(t)$ for SMIB examples.

◁

2.3 Nonlinear Ordinary Differential Equation Model

Suppose the system in (2.1)-(2.6) operates with nominal input $u(t) = u^*(t)$, uncontrolled disturbance $w(t) = w^*(t)$, and parameter $\lambda(t) = \lambda^*(t)$. Let (x^*, y^*) be the nominal trajectory of the system that results from these nominal inputs and parameters with initial conditions $x(t_0) = x_0$ and $y(t_0) = y_0$. The implicit function theorem can be used to establish a connection between the differential-algebraic model and a locally equivalent differential equation model [19].

We assume $h : \mathbb{R}^{n+p+l+q} \mapsto \mathbb{R}^p$ is continuously differentiable at each point $(x, y, w; \lambda)$ of an open set $\mathcal{S} \subset \mathbb{R}^{n+p+l+q}$. Also assume $(x^*, y^*, w^*; \lambda^*) \in \mathcal{S}$ for which the Jacobian matrix $h_y = [\partial h/\partial y]_{(x^*,y^*,w^*;\lambda^*)}$ is nonsingular. By the implicit function theorem [19], in a local neighbourhood of $(x^*, y^*, w^*; \lambda^*)$, there exists a unique function ϕ such that

$$y = \phi(x, w; \lambda), \tag{2.11}$$

and

$$0 = h(x, y, w; \lambda), \tag{2.12}$$

where $(x, y, w; \lambda)$ is in this neighbourhood of $(x^*, y^*, w^*; \lambda^*)$.

Thus, around the nominal system trajectory (x^*, y^*), system (2.1)-(2.6) can be rewritten as

$$\dot{x}(t) = g(x, \phi(x, w; \lambda), u^*; \lambda^*). \tag{2.13}$$

In other words, it is possible to reduce the differential-algebraic model in (2.1)-(2.6) to a differential equation (DE) description of the system model that is valid locally around the nominal trajectory (x^*, y^*). This direct result of the implicit function theorem has been stated before in the context of trajectory sensitivity analysis of power systems [12], [13].

At points where h_y is singular, the conditions of the implicit function theorem are no longer satisfied, so there is no guarantee of the existence of a well-defined $\phi(\cdot)$ in (2.11) [13]. For the power system, the condition is equivalent to the existence of a solution to the AC power flow for $t \in [t_0, T]$. Therefore, in the context of this work, the implicit function theorem is always valid. Thus we can describe the dynamic behaviour of power systems by a nonlinear DE of the form

$$\begin{aligned} \dot{x} &= f(x, u^*, w; \lambda^*), \\ x(t_0) &= x^*(t_0), \\ w(t_0) &= w^*(t_0). \end{aligned} \tag{2.14}$$

***Example* 3** (SMIB)**.** Following the notation in (2.11), it follows from (2.9) that

$$P_e = \phi\left([\delta, \omega]', v_\infty, [E, X_m, X_l, M, D, \omega_s]'\right) = \frac{E v_\infty}{X_l + X_m} \sin\delta. \tag{2.15}$$

Substituting (2.15) into (2.8), we obtain the nonlinear DE description of the dynamic behaviour of the SMIB system, given by

$$\frac{d}{dt}\begin{bmatrix}\delta\\ \omega\end{bmatrix} = \begin{bmatrix}0 & 1\\ 0 & -\frac{D}{M}\end{bmatrix}\begin{bmatrix}\delta\\ \omega\end{bmatrix} + \begin{bmatrix}-1\\ \frac{D}{M}\end{bmatrix}\omega_s + \begin{bmatrix}0\\ -\frac{E}{M(X_m+X_l)}\sin\delta\end{bmatrix}v_\infty + \begin{bmatrix}0\\ \frac{1}{M}\end{bmatrix}T_m.$$

$\lhd$

2.4 Bounding the Disturbance Input

As mentioned in Section 2.2, the disturbance input, $w(t)$, is bounded in some set $\mathcal{W}(t)$ around a nominal $w^*(t)$ during the time horizon of interest $t \in [t_0, T]$. Thus, we rewrite the DE model in (2.14) as

$$\begin{aligned} \dot{x} &= f(x, u^*, w; \lambda^*), \\ x(t_0) &= x^*(t_0), \\ w(t_0) &= w^*(t_0),\ w(t) \in \mathcal{W}(t), \end{aligned} \tag{2.16}$$

where $\mathcal{W}(t)$ represents the deviation of the uncontrolled disturbance $w(t)$ from the nominal $w^*(t)$. If system (2.16) is forward complete, then the solution $x(t)$ exists for $t \in [0, T]$ and it is contained in some set $\mathcal{R}$, which is called the reach set or attainability domain [20], i.e., the set that bounds all possible system trajectories that arise from all possible $w(t) \in \mathcal{W}(t)$. For our studies, this is the set that bounds all possible system trajectories that arise from all possible renewable resource power injection scenarios.

Although the shape of $\mathcal{W}(t)$ is arbitrary, it can always be bounded by an ellipsoid $\Omega_w(t)$ defined as

$$\Omega_w(t) \triangleq \left\{ w(t) : [w(t) - w^*(t)]' Q^{-1}(t) [w(t) - w^*(t)] \leq 1 \right\}, \tag{2.17}$$

such that $\mathcal{W}(t) \subseteq \Omega_w(t)$. Further, the set $\mathcal{W}(t)$ is usually a symmetric polytope. Equivalently, each entry $w_i(t)$ in $w(t)$ is assumed to be confined to some interval, described further in Section 3.3. The interval method has been used in the past for uncertainty modelling in power flow studies [7]. A symmetric polytope can be approximated to a high degree of precision by the

union of a family of ellipsoids. In this case, the reach set $\mathcal{R}$ can be computed for each of the ellipsoids that bounds $\mathcal{W}(t)$. The union of the resulting reach sets for each bounding ellipsoid yields a high-fidelity approximation of the exact reach set $\mathcal{R}$. To simplify subsequent derivations, we assume the uncertain disturbance is indeed bounded by $\Omega_w(t)$, as depicted in Fig. 2.4. Thus, without loss of generality, the system dynamics are described as

$$\begin{aligned} \dot{x} &= f(x, u^*, w; \lambda^*), \\ x(t_0) &= x^*(t_0), \\ w(t_0) = w^*(t_0),\ & w(t) \in \Omega_w(t). \end{aligned} \tag{2.18}$$

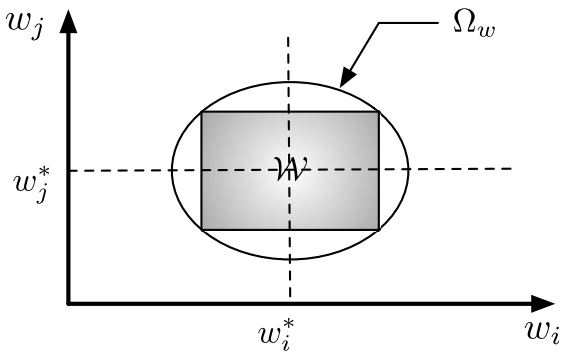

Figure 2.4: $\mathcal{W}$ is bounded by Ω_w.

***Example* 4** (SMIB)**.** We impose an ellipsoidal bound equivalent to $\mathcal{W}_{v_\infty}$ on the disturbance v_∞ and rewrite (2.16) as

$$\begin{aligned} \tfrac{d}{dt}\begin{bmatrix} \delta \\ \omega \end{bmatrix} &= \begin{bmatrix} 0 & 1 \\ 0 & -\frac{D}{M} \end{bmatrix}\begin{bmatrix} \delta \\ \omega \end{bmatrix} + \begin{bmatrix} -1 \\ \frac{D}{M} \end{bmatrix}\omega_s \\ &+ \begin{bmatrix} 0 \\ -\frac{E}{M(X_m+X_l)}\sin\delta \end{bmatrix} v_\infty + \begin{bmatrix} 0 \\ \frac{1}{M} \end{bmatrix} T_m, \\ v_\infty \in \Omega_{v_\infty} &= \left\{ v_\infty : (v_\infty - v_m)\left[(kv_m)^2\right]^{-1}(v_\infty - v_m) \le 1 \right\}. \end{aligned} \tag{2.19}$$

Since v_∞ is one dimensional, $\mathcal{W}_{v_\infty} \equiv \Omega_{v_\infty}$.

2.5 Linearized Model

If the variations in $w(t)$ around $w^*(t)$ are sufficiently small, we can approximate the reach set $\mathcal{R}$ with that of the linearized system denoted as $\Delta\mathcal{R}$. Let $x(t) = x^*(t) + \Delta x(t)$ and $w(t) = w^*(t) + \Delta w(t)$, where $\Delta w(t) \in \Delta\mathcal{W}(t)$ and $\mathcal{W}(t) = w^*(t) \oplus {}^1\Delta\mathcal{W}(t)$. Define $\Delta\mathcal{W}$ such that $\Delta w(t) \in \Delta\mathcal{W}$, for all $t \in [t_0, T]$. Then, $\Delta\mathcal{W}$ represents the worst-case deviation of the uncontrolled disturbance $w(t)$ from the nominal $w^*(t)$. Similar to the argument made for $\mathcal{W}(t)$, the shape of $\Delta\mathcal{W}$ is arbitrary but can always be bounded by an ellipsoid $\Omega_{\Delta w}$ where

$$\Delta w(t) \in \Omega_{\Delta w} = \left\{\Delta w(t) : \Delta w'(t) Q^{-1} \Delta w(t) \leq 1\right\}. \tag{2.20}$$

Let $(x^*, u^*, w^*; \lambda^*)$ be a nominal operating point of system (2.18), where $(x^*, w^*) \in D_x \times D_w$ and $f : [t_0, T] \times D_x \times D_w \mapsto \mathbb{R}^n$ is continuously differentiable with respect to x and w. Then the linearized system, obtained from a first-order Taylor series expansion, is

$$\begin{aligned} \Delta\dot{x} &= A(t)\Delta x + B(t)\Delta w, \\ \Delta x(t_0) &= 0,\ \Delta w(t_0) = 0, \\ \Delta w(t) \in \Omega_{\Delta w} &= \left\{\Delta w(t) : \Delta w'(t) Q^{-1} \Delta w(t) \leq 1\right\}, \end{aligned} \tag{2.21}$$

where the matrices,

$$A(t) = \left.\frac{\partial f(x, u^*, w; \lambda^*)}{\partial x}\right|_{(x^*, w^*)} \tag{2.22}$$

and

$$B(t) = \left.\frac{\partial f(x, u^*, w; \lambda^*)}{\partial w}\right|_{(x^*, w^*)}, \tag{2.23}$$

are the first-order multipliers in the Taylor expansion [19]. We can obtain small variations in system trajectories $\Delta x(t)$ from (2.21).

***Example* 5** (SMIB)**.** We assume the system operates at its stable equilibrium point, i.e., $\delta^* = \delta_0$ and $\omega^* = \omega_0$. For $v_\infty = v_m$, the (stable) equilibrium

[1] $\oplus$ denotes the vector sum of the vector $w^*(t)$ and the set $\Delta\mathcal{W}(t)$.

point of the system (2.16) is given by

$$\begin{aligned} \omega_0 &= \omega_s, \\ \delta_0 &= \sin^{-1}\left(\frac{T_m}{\frac{Ev_m}{X_m+X_l}}\right) \in \left[0, \frac{\pi}{2}\right]. \end{aligned} \tag{2.24}$$

Following the notation in (2.21), we obtain the linearization of the system (2.16) around the equilibrium point in (2.24) as

$$\begin{aligned} \frac{d}{dt}\begin{bmatrix} \Delta\delta \\ \Delta\omega \end{bmatrix} &= \begin{bmatrix} 0 & 1 \\ -\frac{Ev_m}{M(X_m+X_l)}\cos\delta_0 & -\frac{D}{M} \end{bmatrix}\begin{bmatrix} \Delta\delta \\ \Delta\omega \end{bmatrix} + \begin{bmatrix} 0 \\ -\frac{T_m}{Mv_m} \end{bmatrix}\Delta v_\infty, \\ \Delta v_\infty &\in \Omega_{\Delta v_\infty} = \left\{\Delta v_\infty : \Delta v_\infty[(kv_m)^2]^{-1}\Delta v_\infty \leq 1\right\}. \end{aligned} \tag{2.25}$$

$\lhd$

CHAPTER 3

REACH SET CALCULATION

3.1 Linearized Model Reach Set Calculation

Let $\Delta\mathcal{R}(t)$ represent the reach set of (2.21) evolved through time. Then the reach set of (2.21), denoted by $\Delta\mathcal{R}$, containing (for $t \in [t_0, T]$) all possible trajectories of the Δx approximations, is given by

$$\Delta\mathcal{R} = \bigcup_{t=t_0}^{T} \Delta\mathcal{R}(t) = \Delta\mathcal{R}(T), \tag{3.1}$$

since Δx is centered around 0. Also, $\Delta\mathcal{R}(t)$ can be upper bounded with the intersection of a family of ellipsoids:

$$\Delta\mathcal{R}(t) \subseteq \bigcap_{\beta(t)} \mathcal{X}_\beta(t), \ \forall\ \beta(t) \in \mathbb{R} \text{ such that } \beta(t) > 0, \tag{3.2}$$

with $\mathcal{X}_\beta(t) = \{x : x'\Psi_\beta^{-1}(t)x \leq 1\}$, where for each $\beta(t) > 0$, a positive definite $\Psi_\beta(t)$ is obtained by solving

$$\frac{d}{dt}\Psi_\beta(t) = A(t)\Psi_\beta(t) + \Psi_\beta(t)A'(t) + \beta(t)\Psi_\beta(t) + \frac{1}{\beta(t)}B(t)Q(t)B'(t), \tag{3.3}$$

$$\Psi(t_0) = \Psi_0. \tag{3.4}$$

The reader is referred to Appendix A for a derivation of (3.3).

From a practical point of view, simulations would be more easily implemented if $\beta(t)$ were constant, $\beta(t) = \beta_0$. For a stable time-invariant system where $A(t) = A$ and $B(t) = B$, if the differential equation that governs the time evolution of $\Psi_\beta(t)$, (3.3), is stable (more on this in Section 3.2), then we can obtain an upper bound to the steady-state reach set

$\Delta\mathcal{R}_{ss} = \lim_{t\to\infty} \Delta\mathcal{R}(t)$ by solving

$$0 = A\Psi_{\beta_0,ss} + \Psi_{\beta_0,ss}A' + \beta_0\Psi_{\beta_0,ss} + \frac{1}{\beta_0}BQB' \tag{3.5}$$

for $\Psi_{\beta,ss}$. Then

$$\Delta\mathcal{R}_{ss} \subseteq \bigcap_{\beta_0} \mathcal{X}_{\beta_0,ss},\ \forall\ \beta_0 \in \mathbb{R} \text{ such that } \beta_0 > 0,$$

with $\mathcal{X}_{\beta_0,ss} = \{x : x'\Psi^{-1}_{\beta_0,ss}x \leq 1\}$.

***Example* 6** (SMIB)**.** Reachability analysis was performed on the system in (2.25) with the parameter values in Table 2.1. A few ellipsoids of the ellipsoidal family generated via (3.3) centered around the equilibrium point (2.24) are plotted in Fig. 3.1(a) in dashed lines. The intersection of all ellipsoids in the family, depicted with the solid trace in the same figure, represents an upper bound to the reach set of the linearized system (2.25), and also an approximation to the reach set of the nonlinear system.

The same reach set is depicted in Fig. 3.1(b), along with a system trajectory obtained from (2.16). The trajectory results from a scenario where v_∞ jumps between its upper and lower bounds (1.1 and 0.9, respectively) when the norm of the state vector begins to decrease. In terms of excursions of the state variables from the equilibrium point, this represents the worst possible input.

$\lhd$

3.2 Choice of Free Parameter, $\beta(t)$

The matrix differential equation (3.3) defines the matrix $\Psi(t)$, which in turn defines a bounding ellipsoid $\mathcal{X}_\beta(t)$ that contains all possible $x(t)$ for $t \in [t_0, T]$. The differential equation contains a free parameter $\beta(t)$ that produces a bounding ellipsoid for any nonnegative value [17]. Clearly, it would ideal to choose a $\beta(t)$ that is optimal in some sense. Several criteria for optimality have been suggested in the past (see [21], [22], and references therein). For

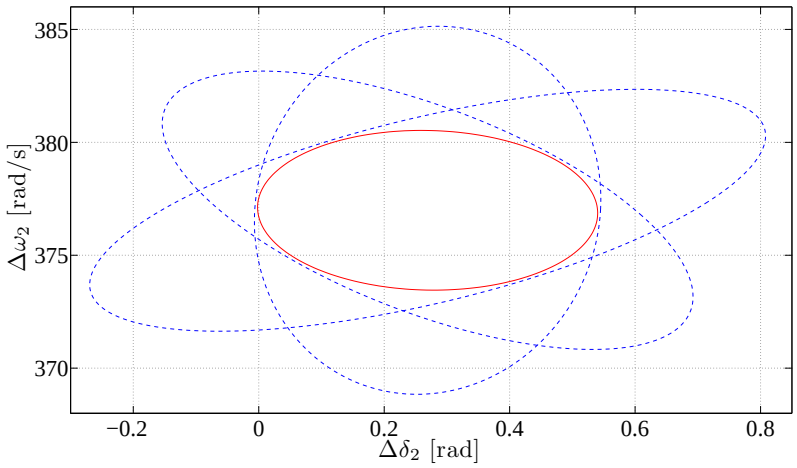

(a) Tight ellipsoidal bounds of the linearized model reach set and reach set obtained as the intersection of the tight ellipsoidal family.

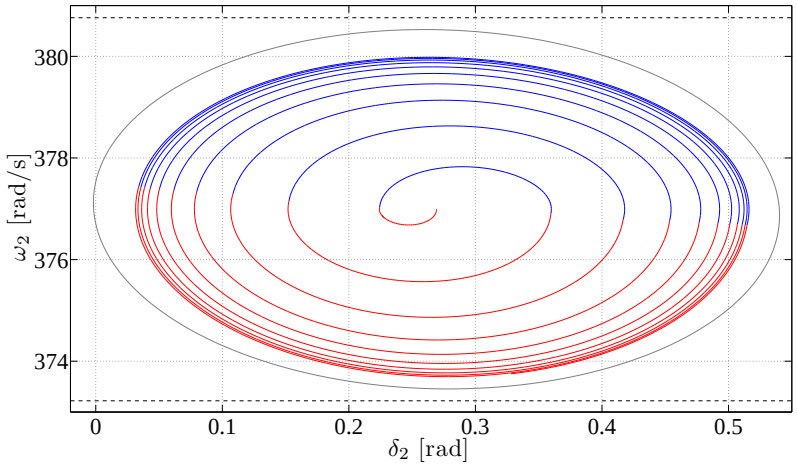

(b) Large-signal worst-case trajectory and linearized model reachability set.

Figure 3.1: Single-machine infinite-bus system reachability analysis results for 10% input uncertainty.

example, we can minimize the volume of the ellipsoid by choosing

$$\beta(t) = \sqrt{\frac{\mathrm{Tr}\left[\Psi^{-1}(t)B(t)Q(t)B'(t)\right]}{n}},$$

and we can minimize the projection of the ellipsoid onto the direction of vector v by choosing

$$\beta(t) = \sqrt{\frac{v'B(t)Q(t)B'(t)v}{v'\Psi(t)v}}. \tag{3.6}$$

If we were interested in the behaviour of only several states in a large-scale system, we may choose $\beta(t)$ that minimizes the projection of the ellipsoid onto a direction that is composed of only those states via (3.6). In order to use this method of selecting $\beta(t)$, however, the system must be controllable [21], which is the ability of an external input to move the internal state of a system from any initial state to any other final state in a finite time interval. For linear time-invariant (LTI) systems of the form,

$$\dot{x} = Ax + Bu,$$

the controllability matrix is $\mathcal{C} = [B \quad AB \quad A^2B \quad \cdots \quad A^nB]$, where n is the dimension of x, the state vector. The LTI system is controllable if and only if $\mathrm{rank}(\mathcal{C}) = n$.

The small-signal models obtained for dynamic power systems as described in (2.21) are not, in general, controllable. Thus, though we may be only interested in the frequency performance of certain synchronous machines, we cannot rely on (3.6) to give optimal ellipsoids based on projections.

3.2.1 Choice of $\beta(t)$ for Uncontrollable Systems

More insight into the effect of $\beta(t)$ may be obtained by rewriting (3.3) into the form

$$\tfrac{d}{dt}\Psi_\beta(t) = \tilde{A}(t)\Psi_\beta(t) + \Psi_\beta(t)\tilde{A}'(t) + B(t)\tilde{Q}(t)B'(t), \tag{3.7}$$

$$\tilde{A}(t) = A(t) + \left[\tfrac{\beta(t)}{2}\right] I, \tag{3.8}$$

$$\tilde{Q}(t) = \left[\tfrac{1}{\beta(t)}\right] Q(t). \tag{3.9}$$

This shows that large $\beta(t)$ tends to make the system that governs $\Psi_\beta(t)$ more unstable, while small $\beta(t)$ tends to amplify the effect of input bound $Q(t)$.

In the subsequent development, we consider the stable time-invariant system $\dot{x} = Ax + Bu$, where a steady-state reach set can be obtained. Also, we consider $\beta(t) = \beta_0$ to be a constant. Then (3.7) becomes

$$\frac{d\Psi_{\beta_0}}{dt} = \tilde{A}\Psi_{\beta_0} + \Psi_{\beta_0}\tilde{A}' + \beta_0\Psi_{\beta_0} + B\tilde{Q}B', \tag{3.10}$$

$$\tilde{A} = A + \left[\tfrac{\beta_0}{2}\right] I, \tag{3.11}$$

$$\tilde{Q} = \left[\tfrac{1}{\beta_0}\right] Q. \tag{3.12}$$

For obvious reasons, we prefer tighter approximations to the reach set. In that sense, we may choose β_0 to be large, so as to reduce the effect of the input uncertainty. On the other hand, we would also like to obtain ellipsoids that do not explode with increasing time. Therefore, β_0 can be chosen to minimize the effect of the input bound while maintaining the stability of (3.7) so that a steady-state Ψ_{ss} is reached as $t \to \infty$. This is the basis of the process by which we choose β_0.

We make use of the Kronecker product in subsequent developments.

Definition 1 (Kronecker product [23])**.** The Kronecker product of $A = [a_{ij}] \in M_{m,n}(\mathbb{F})$ and $B = [b_{ij}] \in M_{p,q}(\mathbb{F})$, where $\mathbb{F}$ is an arbitrary field, is denoted by $A \otimes B$ and is defined to be the block matrix

$$A \otimes B = \begin{bmatrix} a_{11}B & a_{12}B & \dots & a_{1n}B \\ a_{21}B & a_{22}B & \dots & a_{2n}B \\ \vdots & \vdots & \ddots & \vdots \\ a_{m1}B & a_{m2}B & \dots & a_{mn}B \end{bmatrix} \in M_{mp,nq}(\mathbb{F}).$$

$\lhd$

In order to apply the Kronecker product on (3.10), we make use of the following definition:

Definition 2 (Vec$(\cdot)$)**.** With each matrix $A = [a_{ij}] \in M_{m,n}(\mathbb{F})$, we associate the vector $\mathrm{Vec}(A) \in \mathbb{F}^{mn}$ defined by

$$\mathrm{Vec}A \equiv [a_{11}, \dots, a_{m1}, a_{12}, \dots, a_{m2}, \dots, a_{1n}, \dots, a_{mn}]' \tag{3.13}$$

$\lhd$

We can then rewrite (3.10) as follows using Kronecker products:

$$\frac{d}{dt}\text{Vec}\left(\Psi_{\beta_0}\right) = \left(I \otimes \tilde{A} + \tilde{A} \otimes I\right)\text{Vec}\left(\Psi_{\beta_0}\right) + \text{Vec}\left(B\tilde{Q}B'\right). \tag{3.14}$$

The stability of (3.14) depends on the eigenvalues of $\bar{A} = I \otimes \tilde{A} + \tilde{A} \otimes I$. As mentioned earlier, we would like to choose β_0 as large as possible, so as to minimize the effect of the input bound Q, without violating the stability of the system. To determine the eigenvalues of $\bar{A}$, we use the result in the following theorem.

Theorem 1. [23] Let $A \in M_n$ and $B \in M_m$ be given. If $\lambda \in \sigma^1(A)$ and $x \in \mathbb{C}^n$ is a corresponding eigenvector of A, and if $\mu \in \sigma(B)$ and $y \in \mathbb{C}^m$ is a corresponding eigenvector of B, then $\lambda + \mu$ is an eigenvalue of the Kronecker sum $(I_m \otimes A) + (B \otimes I_n)$ and $(y \otimes x) \in \mathbb{C}^{nm}$ is a corresponding eigenvector. Note that $I_m \otimes A$ commutes with $B \otimes I_n$, i.e., $(I_m \otimes A)(B \otimes I_n) = (B \otimes I_n)(I_m \otimes A)$. So, if $\sigma(A) = \{\lambda_1, \ldots, \lambda_n\}$ and $\sigma(B) = \{\mu_1, \ldots, \mu_m\}$, then $\sigma((I_m \otimes A) + (B \otimes I_n)) = \{\lambda_i + \mu_j : i = 1, \ldots, n, j = 1, \ldots, m\}$.

Let $\sigma(\tilde{A}) = \{\tilde{\lambda}_1, \ldots, \tilde{\lambda}_n\}$, and applying the above theorem, we obtain

$$\begin{aligned}\sigma(\bar{A}) &= \sigma(I \otimes \tilde{A} + \tilde{A} \otimes I) \\ &= \{\tilde{\lambda}_i + \tilde{\lambda}_j : i = 1, \ldots, n, j = 1, \ldots, n\}.\end{aligned}$$

From here, it suffices to find the eigenvalue of $\bar{A}$ that has the largest real part and ensure that it is negative. In other words,

$$\max_{i,j}\left\{\text{Re}\left(\tilde{\lambda}_i + \tilde{\lambda}_j\right)\right\} = \max_{i,j}\left\{\text{Re}\left(\tilde{\lambda}_i\right) + \text{Re}\left(\tilde{\lambda}_j\right)\right\} < 0. \tag{3.15}$$

Finally, we relate the eigenvalues of $\tilde{A}$ to those of A through the relationship $\tilde{A} = A + \left[\frac{\beta_0}{2}\right] I$. It can be easily seen that A and $\frac{\beta_0}{2}I$ are commutative. Therefore, there exists a unitary matrix $U \in M_n$ such that $U^*AU = \triangle_A$ is upper triangular, where the eigenvalues of A lie along the diagonal, and

[1] $\sigma(A)$ denotes the eigenvalues of A.

$U^*\left(\frac{\beta_0}{2}I\right)U = \frac{\beta_0}{2}I$. Also, $UU^* = I$. Thus

$$\begin{aligned}\tilde{A} &= A + \frac{\beta_0}{2}I \\ &= U\triangle_A U^* + U\left(\frac{\beta_0}{2}I\right)U^* \\ &= U\left(\triangle_A + \frac{\beta_0}{2}I\right)U^*,\end{aligned}$$

and

$$\sigma(\tilde{A}) = \left\{\tilde{\lambda}_1, \ldots, \tilde{\lambda}_n\right\} = \left\{\lambda_1 + \frac{\beta_0}{2}, \ldots, \lambda_n + \frac{\beta_0}{2}\right\},$$

where $\sigma(A) = \{\lambda_1, \ldots, \lambda_n\}$. Substituting back into (3.15), we obtain

$$\begin{aligned}&\max_{i,j}\left\{\mathrm{Re}\left(\lambda_i + \frac{\beta_0}{2}\right) + \mathrm{Re}\left(\lambda_j + \frac{\beta_0}{2}\right)\right\} \\ =&\max_{i,j}\left\{\mathrm{Re}\left[\lambda_i\right] + \mathrm{Re}\left[\lambda_j\right] + \beta_0\right\} \\ =&\max_{i}\left\{\mathrm{Re}\left[\lambda_i\right]\right\} + \max_{j}\left\{\mathrm{Re}\left[\lambda_j\right]\right\} + \beta_0 < 0,\end{aligned}$$

where $\beta_0 \in \mathbb{R}$. Let

$$\lambda_{\max} = \max_i \mathrm{Re}\left[\lambda_i\right] = \max_j \mathrm{Re}\left[\lambda_j\right],$$

then the condition to ensure stable $\bar{A}$ is

$$\lambda_{\max} + \lambda_{\max} + \beta_0 < 0,$$

or simply,

$$\beta_0 < -2\lambda_{\max}, \tag{3.16}$$

where $\lambda_{\max}$ is the eigenvalue of A with the largest real part. This method of selecting β is depicted in Fig. 3.2.

Alternatively, we can arrive at the same result by solving (3.7) directly

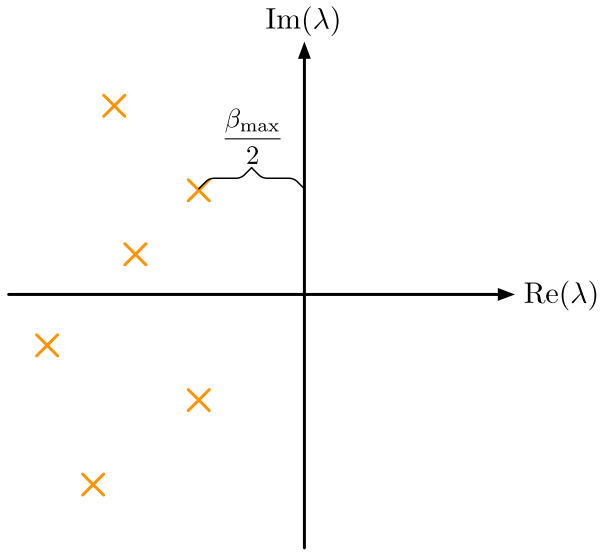

Figure 3.2: The eigenvalues of A, denoted by λ, are all in the open left half complex plane. The maximum value that β_0 can take and still maintain the stability of $\Psi_{\beta_0}(t)$, denoted by βmax, is shown.

with initial condition $\Psi_\beta(t_0)$ [17]. Define

$$\begin{aligned}
\frac{d}{dt}\theta_1(t,t_0) &= \tilde{A}(t)\theta_1(t,t_0),\\
\frac{d}{dt}\theta_2(t,t_0) &= \theta_2(t,t_0)\tilde{A}'(t),\\
\theta_1(t,t) &= I,\\
\theta_2(t,t) &= I.
\end{aligned}$$

Then

$$\Psi_\beta(t) = \theta_1(t,t_0)\left\{\Psi_\beta(t_0) + \int_{t_0}^{t} \theta_1^{-1}(\tau,t_0)B(\tau)\tilde{Q}(\tau)B'(\tau)\theta_2^{-1}(\tau,t_0)d\tau\right\}\theta_2(t,t_0),$$

where $\theta_1(t,t_0) = \exp\left[\tilde{A}(t)(t-t_0)\right]$ and $\theta_2(t,t_0) = \exp\left[\tilde{A}'(t)(t-t_0)\right]$. Thus, stability is achieved if the real parts of the eigenvalues of $\tilde{A}(t)$ lie in the left half plane, which is the same result as (3.16).

The value suggested in (3.16) provides a guideline for the choice of β. We have found it useful to choose β around this stability margin so as to reduce the effect of the input bound Q (which leads to tighter bounding ellipsoid approximations) but also ensure $\Psi_\beta(t)$ does not grow quickly during the time

period in which we are interested. For example, we may be interested in only the reach set of the system for $t < T$.

3.2.2 Choice of $\beta(t)$ for Well-defined Results

Since $\Psi_\beta(t)$ is a matrix that defines the shape and size of an ellipsoid, we require $\Psi_\beta(t)$ to be a positive definite symmetric matrix. In other words, all eigenvalues of $\Psi_\beta(t)$ must be positive. Though past literature has suggested that all nonnegative values of $\beta(t)$ produce bounding ellipsoids [17], we have seen experimentally that $\Psi_\beta(t)$ for some nonnegative values of $\beta(t)$ do not produce valid ellipsoid shape matrices in large power system test cases. This may be due to the ill-conditioning of the A matrix and subsequent numerical errors that may ensue.

Hence, we place an additional constraint on $\beta(t)$ that it must lead to positive definite symmetric $\Psi_\beta(t)$.

3.3 Dynamic Performance Requirements

Dynamic performance requirements generally consist of constraints in the form of interval ranges on variables of interest such as voltage at certain buses and machine frequency deviations. For example, in the Western Electricity Coordinating Council (WECC) system, the acceptable frequency range requirement is between 59.4 Hz and 60.6 Hz [24]. These requirements constrain the excursion of state vector x around x_0 to some region of the state space Φ defined by the symmetric polytope

$$\Phi = \{x : |\pi_i'(x - x_0)| \leq 1 \quad \forall i = 1, 2, \ldots, p\}.$$

The computation of the reach set allows us to determine whether the system violates performance requirements that impose maximum deviations of certain system variables. In fact, verifying that the system meets all dynamic performance requirements for any $w(t) \in \mathcal{W}$ is equivalent to checking that $\Delta\mathcal{R} \subseteq \Phi$.

Example 7 (SMIB)**.** We note that the reach set of the linearized system for 10% input fluctuation is contained within the region defined by the two

horizontal dashed traces in Fig. 3.1(b), which corresponds to the acceptable frequency range of the WECC system. In contrast, neither the linearized system reach set nor the nonlinear system trajectory are contained within the acceptable frequency range for 20% input fluctuation, as shown in Figure 3.3. In fact, the linearized system reach set is contained within the constraints only for input uncertainties of less than 10%. Therefore, the input uncertainty must be less than 10% to conform to the frequency constraint requirement.

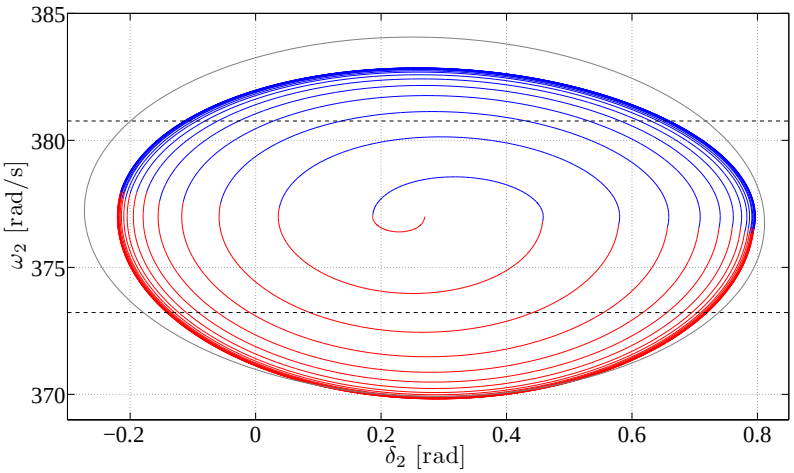

Figure 3.3: Single-machine infinite-bus large-signal worst-case trajectory and linearized model reach set for 20% input uncertainty.

◁

3.4 Note on Small-Signal Approximation

Since the system in (2.21) is a small-signal approximation, even if $\Delta\mathcal{R}$ is the exact reach set of this system, $\Delta\mathcal{R}$ is still just an approximation of the reach set $\mathcal{R}$ for the system (2.14). Thus, in most practical cases, sufficiently accurate results are obtained with the computation of a few ellipsoids of the family in (3.2).

***Example* 8** (SMIB)**.** By inspection of Fig. 3.1(b), the trajectory resulting from the nonlinear system is fully contained within the reach set of the linearized system. Thus, for an input uncertainty of 10%, the reach set of the linearized system is sufficient to estimate that of the nonlinear system

in (2.16). In contrast, the linearized system reach set does not contain the nonlinear system trajectory for worst-case input if the input uncertainty is 20% as depicted in Fig. 3.3. In fact, the trajectory for the worst-case input is contained in the linearized system reach set for input fluctuations of less than 15%.

$\triangleleft$

CHAPTER 4

APPLICATION OF REACHABILITY ANALYSIS TO POWER SYSTEMS

In this chapter, we apply the general reachability notions described in Chapters 2 and 3 to the analysis of power system dynamics.

4.1 Renewable-Based Power Injection

In the most general case, we assume the power injected into the system from renewable-based generation can be modelled as the output of a dynamic or a static system, as depicted in Fig. 4.1. In other words, the process that governs the evolution of a particular resource can be described by differential equations or algebraic equations or a combination thereof. We will elaborate with examples later.

In any given system bus, a power injection can represent a model of a single renewable resource (e.g., a wind farm), or it could represent an aggregated model of several resources (e.g., several wind farms) within the same geographical area.

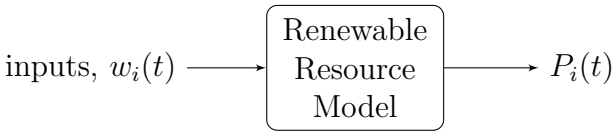

Figure 4.1: Model of general process that governs renewable resource i.

This power injection depends on weather conditions; for example, wind power injection depends on wind speed and photovoltaic power injection depends on irradiation and temperature. Assume the system has r renewable resources or aggregation thereof. For a time horizon $t_0 \leq t \leq T$, let $w_i(t)$ be the uncertain input for the i^{th} resource at time t. Interpretations for $w_i(t)$ include time-evolved wind speed data, solar irradiation, and even power injection into the grid itself. In our model, $w_i(t) \in \mathbb{R}^{l_i}$, where l_i is the number

of uncertain inputs to the process that governs resource i. Thus, to link with ideas presented in Chapter 2, $\sum_{i=1}^{r} l_i = l$ and $w(t) \in \mathbb{R}^l$.

The i^{th}renewable resource can then be modelled by

$$\begin{aligned} \dot{\xi}_i &= F_i \xi_i + G_i w_i + H_i, \\ P_i &= S_i \xi_i + T_i, \end{aligned} \tag{4.1}$$

where $P_i(t)$ represents the power injected by resource i at time $t \in [t_0, T]$. We illustrate this concept with two examples motivated from the work in [15].

***Example* 9** (First-Order Wind Turbine or Aggregate Wind Farm Model)**.** The wind speed at wind resource i is represented by w_i, and $w_i \in \mathbb{R}$. A first-order model for wind farm power output was developed as

$$\begin{aligned} \dot{\xi}_i &= \beta_{i,1} \xi_i + \beta_{i,2} w_i + \beta_{i,3}, \\ P_i &= \xi_i, \end{aligned}$$

where $\xi_i \in \mathbb{R}$. The above is a particular realization of the system described by (4.1). $\lhd$

***Example* 10** (Third-Order Wind Turbine or Aggregate Wind Farm Model)**.** Similarly, a third-order model for wind farm output was derived in [15] as follows:

$$\begin{aligned} \dot{\xi}_i &= \beta_{i,1} \xi_i + \beta_{i,2} w_i + \beta_{i,3}, \\ P_i &= \beta_{i,4} \xi_i + \beta_{i,5}, \end{aligned}$$

where $\xi_i \in \mathbb{R}^3$. Again, this is a realization of (4.1). $\lhd$

4.1.1 Simplification: Fast Dynamics in Renewable Resources

We may make the additional assumption that the dynamics of the renewable resources are much faster than those of conventional generators. As demonstrated in [15], this assumption is valid since the controls in the output power electronics are much faster than machine dynamics. In fact, this is exactly the behaviour of solar generation. In this case, we utilize the standard sin-

gular perturbation model and revise (4.1) as follows:

$$\epsilon\dot{\xi}_i = \tilde{F}_i\xi_i + \tilde{G}_i w_i + \tilde{H}_i, \tag{4.2}$$

$$P_i = S_i\xi_i + T_i, \tag{4.3}$$

where $\tilde{F}_i = \epsilon F_i$, $\tilde{G}_i = \epsilon G_i$, and $\tilde{H}_i = \epsilon H_i$, and $\epsilon << 1$. The revised differential equation degenerates into an algebraic equation as we consider very small ϵ. Then we can rewrite (4.2) as $0 = \tilde{F}_i\xi_i + \tilde{G}_i w_i + \tilde{H}_i$. Solving for ξ_i, we obtain $\xi_i = -\tilde{F}_i^{-1}(\tilde{G}_i w_i + \tilde{H}_i)$. Accordingly, (4.3) becomes $P_i = -S_i\tilde{F}_i^{-1}(\tilde{G}_i w_i + \tilde{H}_i) + T_i$.

4.2 Unknown-but-Bounded Model

Let $w_{i,m}(t) > 0$ be the forecast values of the inputs for the i^{th} renewable resource at time $t \in [t_0, T]$. We assume the actual $w_i(t)$ lies in some confidence band around the predicted nominal $w_i^*(t)$ value. Then each entry of the uncertain input $w_i(t)$, denoted by $w_i^j(t)$, can be described by

$$w_{i,j}(t) \in \mathcal{W}_{i,j}(t) = \left\{|w_{i,j}(t) - w_{i,j}^*(t)| \leq k_{i,j}(t)w_{i,j}^*(t), j \in [1, l_i]\right\}, \tag{4.4}$$

with $i = 1, 2, \ldots, r$, and where $k_{i,j}(t) \geq 0$ depends on the forecast error of $w_{i,j}(t)$ at time $t \in [t_0, T]$.

4.2.1 Simplification: Fast Dynamics in Renewable Resources

Let $P_i(t)$ be the power injected in node i generated from renewable resources at time $t \in [t_0, T]$. Let $P_i^*(t) > 0$ be the forecast values of renewable power injection into node i at time $t \in [t_0, T]$. Then, with the assumptions outlined in 4.1.1, $P_i(t)$ can be described by

$$P_i(t) \in \mathcal{P}_i(t) = \{|P_i(t) - P_i^*(t)| \leq k_i(t)P_i^*(t)\},$$

with $i = 1, 2, \ldots, r$, and where $k_i(t) \geq 0$ depends on the forecast error of the renewable at time $t \in [t_0, T]$. This model is illustrated pictorially in Fig. 4.2. While many realizations are possible for $t \in [t_0, T]$, all are bounded within the forecast error delineated by the dotted traces.

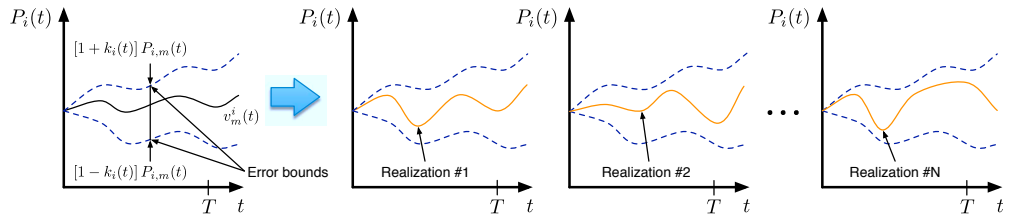

Figure 4.2: Renewable-based power injection model for power injection at node i.

4.3 Linearized Power System Model

Let $\Delta w_i(t) = w_i(t) - w_i^*(t)$ be the variation of the inputs to the renewable resource process around the forecast value $w_i^*(t)$. Then, similar to (4.4),

$$\Delta w_{i,j}(t) \in \Delta \mathcal{W}_{i,j}(t) = \left\{ |\Delta w_{i,j}(t)| \leq k_{i,j}(t) w_{i,j}^*(t), j \in [1, l_i] \right\}.$$

Let $\Delta w(t) = [\Delta w_1(t), \Delta w_2(t), \ldots, \Delta w_r(t)]$ be the vector of uncertain power injections from renewable resources. Then, $\Delta w(t) \in \Delta \mathcal{W}(t)$, where

$$\Delta \mathcal{W}(t) = \Delta \mathcal{W}_1(t) \times \Delta \mathcal{W}_2(t) \times \cdots \times \Delta \mathcal{W}(t), \tag{4.5}$$

is the set of inputs to renewable-based processes.

Then the linearized power system model can be described by augmenting the small-signal power system synchronous machine states Δx with renewable resources states $\Delta \xi_i$ as follows:

$$\begin{aligned}
\Delta \dot{x} &= A\Delta x + B\Delta u, \\
\Delta \dot{\xi}_1 &= F_1 \Delta \xi_1 + G_1 \Delta w_1, \\
&\vdots \\
\Delta \dot{\xi}_i &= F_i \Delta \xi_i + G_i \Delta w_i, \\
&\vdots \\
\Delta \dot{\xi}_r &= F_r \Delta \xi_r + G_r \Delta w_r,
\end{aligned}$$

Let $\Delta\xi = [\Delta\xi_1 \cdots \Delta\xi_i \cdots \Delta\xi_r]'$,

$$F = \begin{bmatrix} F_1 & 0 & \cdots & \cdots & 0 \\ 0 & \ddots & \ddots & & \vdots \\ \vdots & \ddots & F_i & \ddots & \vdots \\ \vdots & & \ddots & \ddots & 0 \\ 0 & \cdots & \cdots & 0 & F_r \end{bmatrix},$$

and

$$G = \begin{bmatrix} G_1 & 0 & \cdots & \cdots & 0 \\ 0 & \ddots & \ddots & & \vdots \\ \vdots & \ddots & G_i & \ddots & \vdots \\ \vdots & & \ddots & \ddots & 0 \\ 0 & \cdots & \cdots & 0 & G_r \end{bmatrix}.$$

We can rewrite the augmented model in matrix form as

$$\begin{bmatrix} \Delta\dot{x} \\ \Delta\dot{\xi} \end{bmatrix} = \begin{bmatrix} A & 0 \\ 0 & F \end{bmatrix} \begin{bmatrix} \Delta x \\ \Delta\xi \end{bmatrix} + \begin{bmatrix} B & 0 \\ 0 & G \end{bmatrix} \begin{bmatrix} \Delta u \\ \Delta w \end{bmatrix},$$
$$\Delta x(t_0) = x_0, \quad \Delta\xi(t_0) = \xi_0,$$
$$\Delta w(t) \in \Delta\mathcal{W}(t). \tag{4.6}$$

4.3.1 Simplification: Fast Dynamics in Renewable Resources

Here, we make the same simplifying assumptions as in Section 4.1.1. Let $\Delta P_i(t) = P_i(t) - P_i^*(t)$ be the variation of renewable-based power injection around the forecast value $P_{i,m}(t)$. Then

$$\Delta P_i(t) \in \Delta\mathcal{P}_i(t) = \{|\Delta P_i(t)| \leq k_i(t) P_i^*(t)\}. \tag{4.7}$$

Let $\Delta P(t) = [\Delta P_1(t), \Delta P_2(t), \ldots, \Delta P_r(t)]$ be the vector of uncertain power injections from renewable resources. Then, $\Delta P(t) \in \Delta\mathcal{P}(t)$, where

$$\Delta\mathcal{P}(t) = \Delta\mathcal{P}_1(t) \times \Delta\mathcal{P}_2(t) \times \cdots \times \Delta\mathcal{P}_r(t) \tag{4.8}$$

is the set of renewable-based power injections. This is illustrated in Fig. 4.3 for the case of power injection at nodes i and j. Then, assuming the power

injection model of (4.7) and (4.8), the linearized power system model can be described by

$$\begin{aligned} \tfrac{d\Delta x}{dt} &= A\Delta x + B\Delta P, \\ \Delta x(t_0) = 0, \quad \Delta P(t) &\in \Delta\mathcal{P}(t). \end{aligned} \tag{4.9}$$

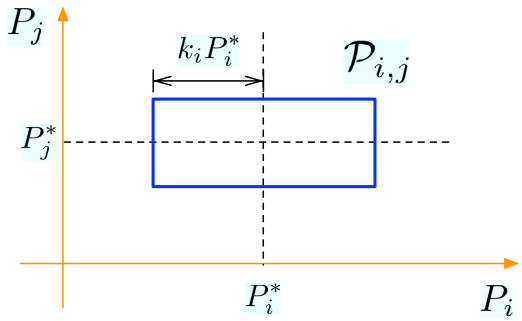

Figure 4.3: Renewable-based power injection model for power injection at nodes i and j.

4.4 Comparison Between Two Renewable-Based Power Injection Models

In this chapter, we discussed two methods with which we model renewable power injections. The first models a renewable resource as a dynamic system, where the input to that system is unknown-but-bounded. On the other hand, the second models a renewable resource as a static system, where the power injected into the power system is unknown-but-bounded. In Chapter 6, we make use of both models on large-scale power systems and discuss the ramifications of these models with respect to specific test cases. Here, we provide some intuition on the difference between the two models and draw some connections to physical systems.

In the simplified model, where we bound the renewable power injection directly, the intuition is quite straightforward. This power injection is viewed as a negative load; all dynamics of the renewable generation system are neglected. We assume the power injection varies freely between the lower and upper bounds. For example, the power injected can make quite sudden

step changes or can be quite slowly ramping, as long as it is within the assumed bounds. We consider only the dynamics of the power system.

For the case in which we model the renewable resource as a dynamic system, as in (4.1), by bounding the system input, we are effectively bounding the rate at which the states change. For example, consider the first-order wind turbine model in Example 9, $w_i \in \mathcal{W}_i$ and $\xi_i(0) = P_i(0) \in \mathcal{P}_i(0)$; then $\dot{\xi}_i = \dot{P}_i$ is bounded. This can be seen by following a similar argument as in Appendix A if we assume $\mathcal{W}_i$ and $\mathcal{P}_i(0)$ are indeed ellipsoids. Thus, this model assumes a bound not only on the renewable system input but also on the ramp rate of its states.

4.5 Reach Set Computation

By definition, $\Delta\mathcal{W}(t)$ is an l-dimensional symmetrical polytope centered around zero. Thus, the ellipsoidal techniques presented in Section 3.1 cannot be directly used to compute the reach set of (4.6). As discussed before, we can circumvent this problem by bounding the polytope $\Delta\mathcal{W}(t)$ by an ellipsoid that is the minimum volume ellipsoid containing the set of all possible realizations of the inputs $\Delta w(t)$. Then ellipsoidal techniques can be used to compute an upper-bound on the reach set of (4.6). If a more accurate reach set is required, $\Delta\mathcal{W}(t)$ can be represented as the intersection of a family of ellipsoids, each of which is tight to $\Delta\mathcal{W}(t)$ in a specific direction.

An analogous technique can be applied to $\Delta\mathcal{P}(t)$ to compute an upper-bound on the reach set of (4.9).

4.6 Reach Set Visualization

In general, the reach set calculated above is a multi-dimensional ellipsoid and is therefore difficult to visualize. Fortunately, we are usually only concerned with a few variables, such as the electrical speed or angle of a synchronous machine. Thus, we can project the multi-dimensional ellipsoidal reach set onto the space that is composed of the two variables in which we are interested. The reader can refer to Appendix B for more details. This is the technique we utilize to visualize reach sets later in Chapter 6.

CHAPTER 5

THREE-BUS SYSTEM WITH CONVENTIONAL AND RENEWABLE-BASED POWER GENERATION

The development described in Chapters 2–4 are applied to a a simple three-bus system as depicted in Fig. 5.1. In this system, a synchronous machine is connected to bus 1. As in the SMIB example, a classical model is used to describe the machine dynamics, but this model is augmented with an additional equation to describe the governor model so that the mechanical torque T_m becomes a third state variable and the valve position P_c becomes an external reference. Renewable-based power is injected at bus 2 and the load at bus 3 is served by both conventional and renewable generation.

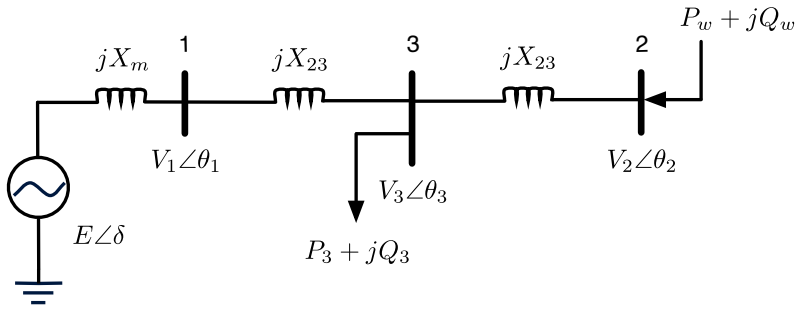

Figure 5.1: Three-bus system with renewable-based power injection.

The synchronous machine model connected to bus 1 is given by $\dot{x} = g(x, y, u; \lambda)$ in the notation of (2.1) or

$$\frac{d}{dt}\begin{bmatrix} \delta \\ \omega \\ T_m \end{bmatrix} = \begin{bmatrix} 0 & 1 & 0 \\ 0 & -\frac{D}{M} & \frac{1}{M} \\ 0 & -\frac{1}{T_{SV}R_D\omega_s} & -\frac{1}{T_{SV}} \end{bmatrix}\begin{bmatrix} \delta \\ \omega \\ T_m \end{bmatrix} + \begin{bmatrix} 0 \\ -\frac{EV_1}{MX_m}\sin(\delta - \theta_1) \\ 0 \end{bmatrix} + \begin{bmatrix} -1 \\ \frac{D}{M} \\ \frac{1}{\omega_s T_{SV} R_D} \end{bmatrix}\omega_s + \begin{bmatrix} 0 \\ 0 \\ \frac{1}{T_{SV}} \end{bmatrix} P_c. \tag{5.1}$$

The renewable-based power generation injection model at bus 2 is given by

$$\begin{aligned} P_w(t) \in \mathcal{P}_w = \{P_w : |P_w - P_m| \leq k_w P_m\}, \\ Q_w(t) = Q_w, \end{aligned} \tag{5.2}$$

where we assume the forecasted power injection $P^*(t) = P_m$ into bus 2, forecast error k_w, and deterministic input Q_w are constants. We now turn our attention to the algebraic power balance equation $0 = h(x, y, w; \lambda)$ in (2.2). The power balance equations for bus 2 are given by

$$h_1 = P_w = Y_{23} V_2 V_3 \sin(\theta_2 - \theta_3), \tag{5.3}$$

$$h_2 = Q_w = Y_{23} V_2^2 - Y_{23} V_2 V_3 \cos(\theta_2 - \theta_3). \tag{5.4}$$

The power balance equations for bus 1 are given by

$$\begin{aligned} h_3 =& Y_{13} V_1 V_3 \sin(\theta_1 - \theta_3) \\ & - Y_m E V_1 \sin(\delta - \theta_1) = 0, \end{aligned} \tag{5.5}$$

$$\begin{aligned} h_4 =& (Y_{13} + Y_m) V_1^2 - Y_{13} V_1 V_3 \cos(\theta_1 - \theta_3) \\ & + Y_m V_1^2 - Y_m E V_1 \cos(\delta - \theta_1) = 0. \end{aligned} \tag{5.6}$$

The power balance equations for bus 3 are given by

$$\begin{aligned} h_5 =& Y_{13} V_1 V_3 \sin(\theta_3 - \theta_1) \\ & + Y_{23} V_2 V_3 \sin(\theta_3 - \theta_2) + P_3 = 0, \end{aligned} \tag{5.7}$$

$$\begin{aligned} h_6 =& (Y_{13} + Y_{23}) V_3^2 - Y_{13} V_1 V_3 \cos(\theta_3 - \theta_1) \\ & - Y_{23} V_2 V_3 \cos(\theta_3 - \theta_2) + Q_3 = 0. \end{aligned} \tag{5.8}$$

5.1 Small-Signal Model

Define $\theta_1' := \theta_1 - \delta$, $\theta_2' := \theta_2 - \delta$, $\theta_3' := \theta_3 - \delta$, $\theta_{13}' := \theta_1' - \theta_3'$, $\theta_{23}' := \theta_2' - \theta_3'$. Then, the small-signal model that results from linearizing (5.1) – (5.8) is given by

$$\frac{d}{dt} \begin{bmatrix} \Delta\omega \\ \Delta T_m \end{bmatrix} = A_m \begin{bmatrix} \Delta\omega \\ \Delta T_m \end{bmatrix} + B_m \begin{bmatrix} \Delta V_1 \\ \Delta\theta_1' \end{bmatrix}, \tag{5.9}$$

where

$$A_m = \begin{bmatrix} -\frac{D}{M} & \frac{1}{M} \\ -\frac{1}{T_{SV} R_D \omega_s} & -\frac{1}{T_{SV}} \end{bmatrix},$$
$$B_m = \begin{bmatrix} \frac{E}{MX_m} \sin\theta'_{1o} & \frac{EV_{1o}}{MX_m} \cos\theta'_{1o} \\ 0 & 0 \end{bmatrix}, \tag{5.10}$$

and

$$\begin{bmatrix} \Delta P_w \\ \Delta Q_w \\ 0 \\ 0 \\ 0 \\ 0 \end{bmatrix} = \begin{bmatrix} 0 & C_{12} \\ C_{21} & C_{22} \end{bmatrix} \begin{bmatrix} \Delta V_1 \\ \Delta\theta'_1 \\ \Delta V_2 \\ \Delta V_3 \\ \Delta\theta'_{13} \\ \Delta\theta'_{23} \end{bmatrix}, \tag{5.11}$$

where

$$C_{12} = \left[\frac{\partial h_a}{\partial x_2}\right], \quad C_{21} = \left[\frac{\partial h_b}{\partial x_1}\right], \quad C_{22} = \left[\frac{\partial h_b}{\partial x_2}\right], \tag{5.12}$$

and $h_a = [\ h_1 \quad h_2\ ]'$, $h_b = [\ h_3 \quad h_4 \quad h_5 \quad h_6\ ]'$, $x_1 = [\ V_1 \quad \theta'_1\ ]'$, $x_2 = [\ V_2 \quad V_3 \quad \theta'_{13} \quad \theta'_{23}\ ]'$, and where ΔP_w is given by

$$\Delta P_w \in \Delta\mathcal{P}_w = \{\Delta P_w : |\Delta P_w| \leq k_w P_m\},$$
$$\Delta Q_w = 0. \tag{5.13}$$

Then, following the notation of (2.21), the small-signal model can be rewritten as

$$\frac{d}{dt}\begin{bmatrix} \Delta\omega \\ \Delta T_m \end{bmatrix} = A \begin{bmatrix} \Delta\omega \\ \Delta T_m \end{bmatrix} + B \begin{bmatrix} \Delta P_w \\ \Delta Q_w \end{bmatrix}, \tag{5.14}$$

where $A = A_m$, and $B = -B_m(C_{12}C_{22}^{-1}C_{21})^{-1}$.

Table 5.1: Three-Bus System Model Parameter Values

P_3	Q_3	P_m	Q_w	X_{13}	X_{23}	X_m	M	D [s/rad]	T_m	ω_s [rad/s]	k_w	T_{SV}	R_D
1	0.5	0.4	0	0.1	0.15	0.2	$\frac{1}{15\pi}$	0.04	1	120π	0.3	0.2	0.05

5.2 Reachability Numerical Analysis

Reachability analysis of system (5.14) was conducted using the parameter values in Table 5.1. A steady-state power flow study was conducted to obtain all the equilibrium voltage magnitudes and angles needed in the linearized model, which yielded the following results: $E_{1o} = 1.13$ p.u., $V_{1o} = 1$ p.u., $V_{2o} = 0.94$ p.u., $V_{3o} = 0.94$ p.u., $\theta'_{1o} = -6.12°$, $\theta'_{13o} = 3.65°$, $\theta'_{23o} = 3.89°$. A few ellipsoids of the ellipsoidal family generated via (3.3) centered around the equilibrium point of the linearized system are plotted in Fig. 5.2. The true reach set for the linearized system (5.14) is the intersection of the family of ellipsoids. Here, the reach set is the result of 30% variation in P_w around the nominal value. By visual inspection, we note that the reach set is entirely contained within the region defined by the solid vertical traces, which, as before, represent the acceptable frequency range of the WECC system.

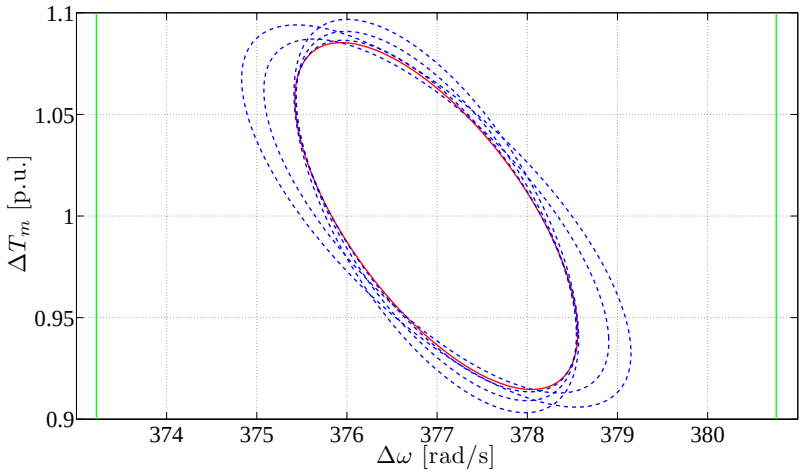

Figure 5.2: Three-bus system reachability analysis results

CHAPTER 6

CASE STUDIES

In this chapter, we apply the methodology described in Chapters 2–4 to several benchmark cases: the Western Electric Coordinating Council (WECC) system, the New England system, and the Northeast Power Coordinating Council (NPCC) system. To that end, we modified the MATLAB-based Power Systems Toolbox (PST) small-signal stability analysis capability to our needs. PST is capable of performing linearization around a steady-state operating point to produce a linear system of the form of $\Delta\dot{x} = A\Delta x + B\Delta u$. Additionally, we developed custom-made MATLAB-based code that implements ellipsoidal-based reach set calculations. We mimic the integration of renewable resources by displacing certain synchronous generators in the system with alternative generation. Then the modified system is subject to uncertain wind speed or real power input and over-approximations to the linearized system reach set are obtained. The reader is referred to Appendix C for more implementation details.

6.1 WECC 3-Machine Test Case

We apply reachability analysis to a simplified WECC system model, which consists of three generators and nine buses. To mimic the effect of power injection from renewable resources, we replace the generator at bus 3 with a negative load as depicted in Fig. 6.1(a). Each synchronous machine is modelled with the two-axis machine (4 states each) with exciters (3 states each), more details of which can be found in [16]. Hence, the state variables for each machine are

$$\Delta x_i = \begin{bmatrix} \Delta\delta_i & \Delta\omega_i & \Delta E'_{q_i} & \Delta E'_{d_i} & \Delta V_{R_i} & \Delta E_{fd_i} & \Delta R_{f_i} \end{bmatrix}', \tag{6.1}$$

where $i = 1, 2, 3$, and the last three states are related to the exciter. Hence there are 21 dynamic states in the system prior to modification.

Referring to Fig. 6.1(a), Q_w represents the reactive power injection at bus 3 and is a constant deterministic input. We also assume the nominal realization of the uncertain input $P_w(t)$, the real power injection at bus 3, is constant in the time horizon of interest so that $P_w^*(t) = P_m > 0$. Then $P_w(t)$ is bounded within some neighbourhood of P_m, more specifically,

$$P_w(t) \in \mathcal{P}(t) = \{P_w : |P_w - P_m| \leq k\},$$

where we assume $k > 0$ is a constant. Let $\Delta P_w(t) = P_w(t) - P_m$. Then

$$\Delta P_w(t) \in \Delta\mathcal{P}(t) = \{\Delta P_w : |\Delta P_w| \leq k\}.$$

Since $P_w(t)$ is one-dimensional, $\Delta\mathcal{P}(t)$ is, in fact, an ellipsoid.

PST's small-signal analysis tool is used to linearize the system in Fig. 6.1(a) around its operating point, as dictated by the AC power flow, to obtain a system of the form $\Delta\dot{x} = A\Delta x + B\Delta P_w$, where $\Delta x(0) = 0$. Also, we choose $k = 0.1$ so that $|\Delta P_w(t)| \leq 0.1$ for $t \in [0, T]$.

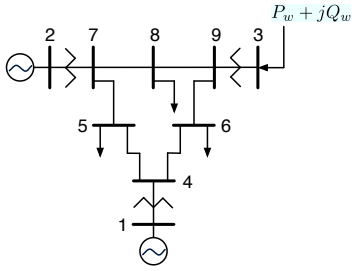

(a) Simplified WECC system with renewable-based power injection.

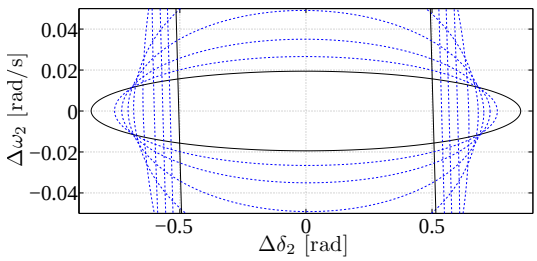

(b) Reach set of $\Delta\omega$-$\Delta\delta$ for the generator at bus 2 with ± 0.1 p.u. input ΔP_w uncertainty.

Figure 6.1: Simplified WECC linearized model with uncertainty in P_w.

Several ellipsoids are generated using (3.3) for various values of $\beta > 0$. The results are depicted in Fig. 6.1(b) with the dashed trace for $T = 200$ s. In the same figure, the true reach set for the linearized system is upper bounded by the intersection of the solid traces. We deduce that the angular position of generator 2 does not deviate more than approximately 0.5 rad from its nominal value, while the angular speed of the same generator does not deviate more than approximately 0.02 rad/s from its nominal value.

Table 6.1: Machines Replaced with Renewable Resources in New England System Test Cases

Uncertainty Model	20% renewable		30% renewable	
	Case A	Case B	Case A	Case B
Negative load	Machines 2, 4	Machines 6, 8	Machines 9, 10	Machines 3, 6, 7
1^{st}-order wind farm model	Machines 2, 4	Machines 6, 8	Machines 9, 10	Machines 3, 6, 7

6.2 New England 10-Machine Test Case

The New England test case contains 39 buses and 10 synchronous machines. Each machine is modelled with the two-axis machine (4 states each); all but the tenth machine are modelled with exciters (3 states each). Hence, the state variables for each machine (except the tenth) are as in (6.1). The state variables for the 10^{th} machine are

$$\Delta x_i = \begin{bmatrix} \Delta\delta_i & \Delta\omega_i & \Delta E'_{q_i} & \Delta E'_{d_i} \end{bmatrix}', \tag{6.2}$$

where $i = 10$. Thus, prior to modifications, this system has 67 dynamic states.

According to the system data found in PST, this test system has a generating capacity of 61.9293 p.u. We perform our reachability studies by replacing certain synchronous generators with alternative resources to achieve 20% and 30% renewable penetration. This ensures the system reaches the same power flow solution as before the replacement. The test cases are described in Table 6.1, where each entry denotes the synchronous machines that are replaced by renewable resources.

In the reach set plots that appear in Figs. 6.2-6.8, we present several ellipsoids obtained from choosing different values of β, as described in Chapter 3 at $t = T = 60$ s. Each ellipsoid bounds the exact reach set of the linearized system. The intersection of the ellipsoids provides a tighter bound on that set and gives an approximation to the reach set of the nonlinear power system. To visualize the reach set, we choose two variables of interest and project the ellipsoidal reach sets onto the subspace that contains those two variables, as described in Chapter 4.

We consider two uncertainty models as described in Chapter 4. In the first model, the unknown-but-bounded uncertainty is associated with the

power injected into the grid from renewable resources. Again, we assume the nominal power injected is a constant for the time period of interest. Then, $\Delta P \in \Delta\mathcal{P}$, where $\Delta P = [\Delta P_1 \quad \Delta P_2 \quad \cdots \quad \Delta P_r]$, and r is the number of renewable resources in the system. While the shape of $\Delta\mathcal{P}(t)$ is arbitrary, we define ellipsoid $\Delta\Omega_P$ such that $\Delta\mathcal{P}(t) \subseteq \Delta\Omega_P$ for all $t \in [t_0, T]$, where

$$\Delta\Omega_P = \{\Delta P : \Delta P' Q_P^{-1} \Delta P \leq 1\}.$$

For the second model, we assume the alternative resources are identical first-order wind farms, as in Example 9, with $\beta_1 = -0.1761$, $\beta_2 = 0.0134$, and $\beta_3 = -0.0979$. Then, for the i^{th} wind farm,

$$\Delta\dot{P}_i = -0.1761\Delta P_i + 0.0134\Delta w_i, \tag{6.3}$$

where Δw_i is the variation of the wind speed at wind farm site i around some nominal value, assumed to be constant. Then, $\Delta w \in \Delta\mathcal{W}$, where $\Delta w = [\Delta w_1 \quad \Delta w_2 \quad \cdots \quad \Delta w_r]$ and r is the number of renewable resources in the system. Similarly to the unknown-but-bounded power model, we define an ellipsoid $\Delta\Omega_w$ such that $\Delta\mathcal{W}(t) \subseteq \Delta\Omega_w$ for all $t \in [t_0, T]$, where

$$\Delta\Omega_w = \{\Delta w : \Delta w' Q_w^{-1} \Delta w \leq 1\}.$$

6.2.1 20% Renewable Penetration

In this section, we investigate the reachability of the linearized New England system with 20% renewable penetration. We mimic the desired level of penetration by replacing machines 2 and 4 in case A and machines 6 and 8 in case B with renewable resources.

A: Machines 2 and 4

We consider the case where machines 2 and 4 are replaced with renewable resources. These two synchronous machines account for 19.5% of the total generation in the New England test case. Reachability results are shown in Figs. 6.2 and 6.3.

In Fig. 6.2(a), we assume the renewable power injections are known within

± 0.2 p.u. of their nominal values, i.e., the values at which the system was linearized. On the other hand, we assume the first-order wind farm model in Fig. 6.2(b), where the wind speeds at the two sites are known within ± 0.2m/s of their nominal value. As expected, the reach set for the case of unknown-but-bounded wind speeds is much smaller. As mentioned previously, the unknown-but-bounded wind speeds, in effect, bound the ramp rates of the power injection. Therefore, the conditions that led to the result depicted in Fig. 6.2(a) represent more stringent constraints on the input.

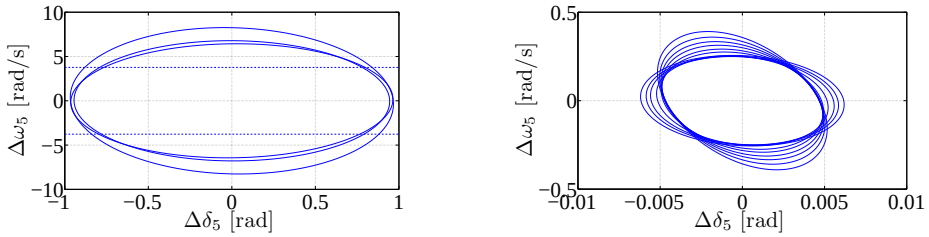

(a) Unknown-but-bounded ΔP_2 and ΔP_4. (b) Unknown-but-bounded Δw_2 and Δw_4.

Figure 6.2: Reachability results for machine 5 in the New England test case with replacement of machines 2 and 4, 20% renewable penetration, and ± 0.2 input uncertainty.

Similar results are obtained when we consider the angle and frequency of machine 3, whose reach sets are depicted in Fig. 6.3. We see that with the additional approximate wind farm dynamics, the deviation $\Delta\omega_3$ from its nominal value is about an order of magnitude smaller than that obtained from bounding the magnitudes of power injections only. In fact, the frequency deviations, depicted in Figs. 6.2(a) and 6.3(a), would exceed the maximum allowable frequency deviation for the WECC system. Thus, in the subsequent New England test cases, we opt to present the results obtained from the more detailed model containing wind farm dynamics.

We can visualize the resulting reach set by projecting the multi-dimensional ellipsoid onto the speeds of two synchronous machines, as depicted in Fig. 6.4. We deduce that while the frequencies of each machine can vary individually between -0.1 rad/s and 0.1 rad/s around the nominal value, their variations are correlated. For example, it is not possible to have one machine deviate its nominal value by 0.1 rad/s, while the other deviates by -0.1 rad/s. This technique would be advantageous to establish the existence and degree of correlation between certain variables.

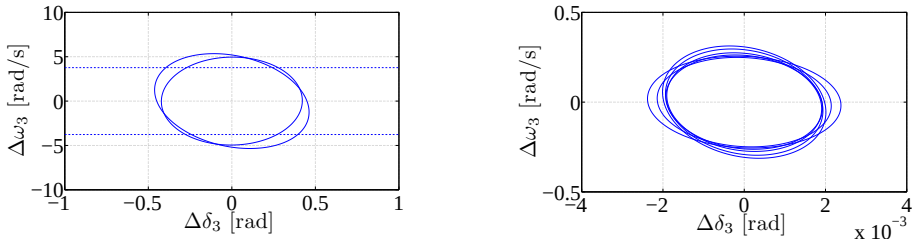

(a) Unknown-but-bounded ΔP_2 and ΔP_4. (b) Unknown-but-bounded Δw_2 and Δw_4.

Figure 6.3: Reachability results for machine 3 in the New England test case with replacement of machines 2 and 4, 20% renewable penetration, and ± 0.2 input uncertainty.

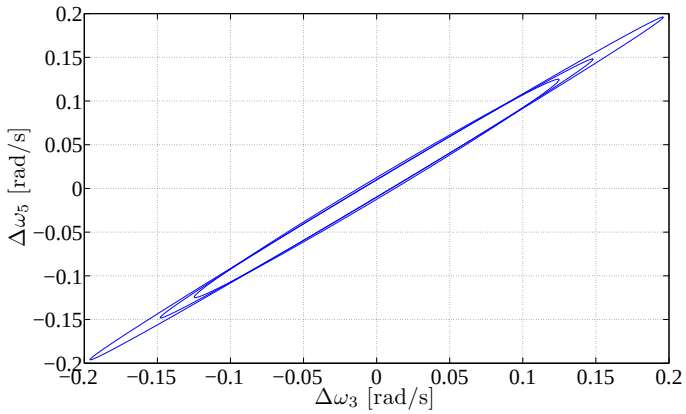

Figure 6.4: Reachability results for machine frequency in the New England test case with replacement of machines 2 and 4, 20% renewable penetration, and ± 0.1 m/s wind speed uncertainty.

B: Machines 6 and 8

The combined generation of machines 6 and 8 accounts for 19.4% of the system's total generation. Here, we illustrate the effect of the degree of input variability on the reach set as depicted in Fig. 6.5. We conduct the simulation with the first-order wind farm model with varying input wind speed uncertainty at the two locations. For example, for the case depicted in Fig. 6.5(b),

$$\Delta w \in \Delta\Omega_{\Delta w} = \left\{ \Delta w : \Delta w' \begin{bmatrix} 0.09 & 0 \\ 0 & 0.09 \end{bmatrix}^{-1} \Delta w \leq 1 \right\},$$

where $\Delta w \in \mathbb{R}^2$, so that the input wind speeds at both wind farm sites are known within ± 0.3 m/s of the nominal forecasted values.

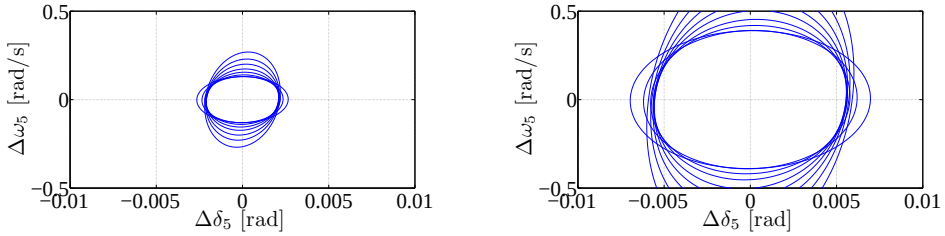

(a) ± 0.1 m/s input uncertainty.

(b) ± 0.3 m/s input uncertainty.

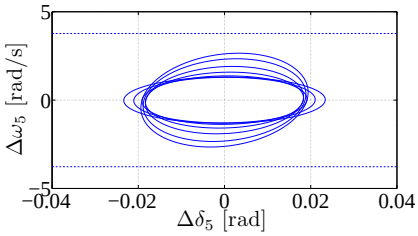

(c) ± 1 m/s input uncertainty.

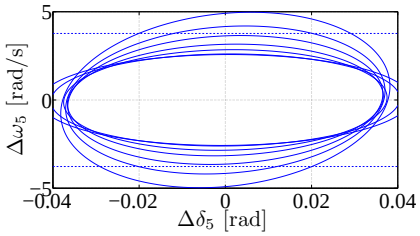

(d) ± 2 m/s input uncertainty.

Figure 6.5: Reachability results for machine 5 in the New England test case with replacement of machines 6 and 8, 20% renewable penetration, first-order wind farm models for the renewable resources, and unknown-but-bounded model for wind speeds.

Again, each ellipsoid shown is the projection of a bounding ellipsoid to the exact reach set, and their intersection represents a tighter bound. We see the approximate reach set composed of the speed and angle of synchronous machine 5 grows with increased input uncertainty, as expected. The dashed lines in Figs. 6.5(c) and 6.5(d) denote the frequency constraints in the WECC system. As illustrated, the frequency constraint is not violated even for wind speed input uncertainty of ± 2 m/s.

The ellipsoids bounding the reach set are projected onto the subspace that is composed of ω_7 and ω_2 as shown in Fig. 6.6. Similar conclusions can be drawn for the correlation between ω_7 and ω_2 as for ω_5 and ω_3 in the previous test case. The dashed lines in Fig. 6.6 indicate the WECC frequency constraint requirement. With ± 2 m/s input variability, machines 2 and 7 are much closer to violating that constraint simultaneously than machines 3 and 5 in the previous test case with ± 0.1 m/s input uncertainty.

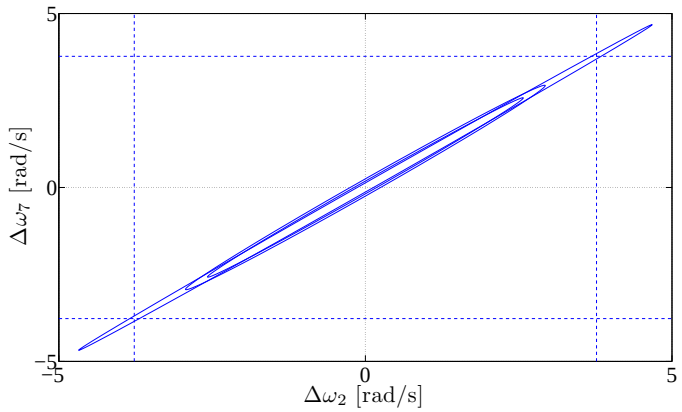

Figure 6.6: Reachability results for machine frequency in the New England test case with replacement of machines 6 and 8, 20% renewable penetration, and ±2 m/s wind speed uncertainty.

6.2.2 30% Renewable Penetration

In this section, we investigate the reachability of the linearized New England system with 30% renewable penetration. We mimic the desired level of penetration by replacing machines 9 and 10 in case A and machines 3, 6 and 8 in case B with renewable resources. We present results of only the case where the dynamics of the wind farm have been included with the first-order approximation and the unknown-but-bounded inputs are the wind speeds at respective sites.

A: Machines 9 and 10

The combined generation of machines 9 and 10 accounts for 29.5% of the system's total generation. Reachability results are shown in Fig. 6.7 for machine 5. As expected, the deviations of state variables $\Delta\omega_5$ and $\Delta\delta_5$ grow with increasing input uncertainty.

B: Machines 3, 6, 7

The combined generation of machines 6 and 8 accounts for 30.0% of the system's total generation. Reachability results are shown in Fig. 6.8 for machine 5.

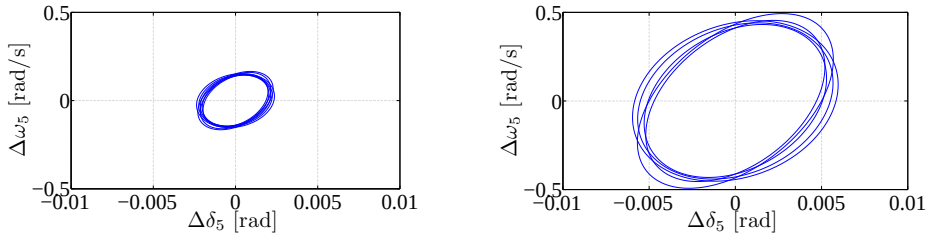

(a) ±0.1 m/s input uncertainty.

(b) ±0.3 m/s input uncertainty.

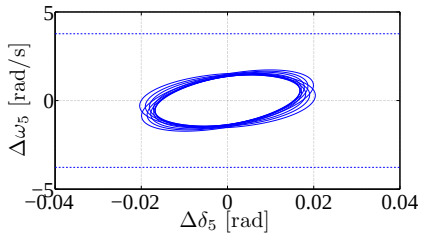

(c) ±1 m/s input uncertainty.

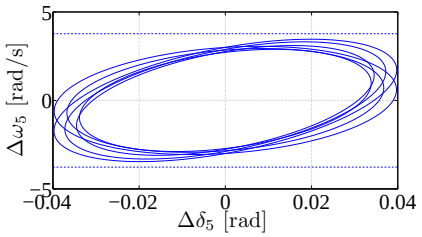

(d) ±2 m/s input uncertainty.

Figure 6.7: Reachability results for machine 5 in the New England test case with replacement of machines 9 and 10, 30% renewable penetration, first-order wind farm models for the renewable resources, and unknown-but-bounded model for wind speeds.

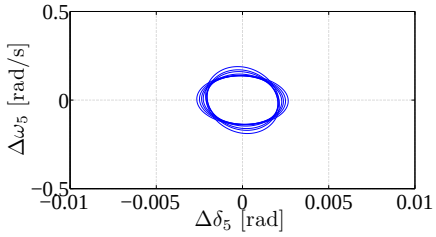

(a) ±0.1 m/s input uncertainty.

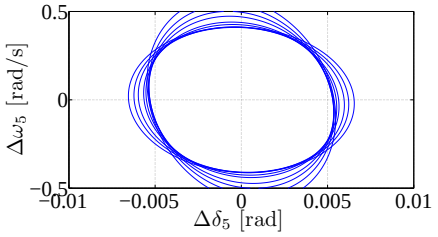

(b) ±0.3 m/s input uncertainty.

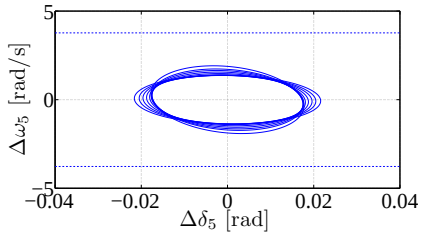

(c) ±1 m/s input uncertainty.

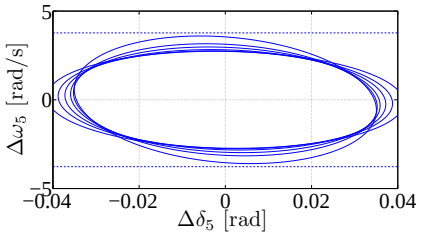

(d) ±2 m/s input uncertainty.

Figure 6.8: Reachability results for machine 5 in the New England test case with replacement of machines 3, 6, and 7, 30% renewable penetration, first-order wind farm models for the renewable resources, and unknown-but-bounded model for wind speeds.

Cases A and B, for which reachability results are depicted in Figs. 6.7 and 6.8, respectively, both represent a renewable penetration of about 30%. Thus, we expect the state variable deviations to be about the same between the two cases, which we observe by visual inspection of Figs. 6.7 and 6.8. However, in a later example, we find that the resulting variations in system variables are vastly different when we compare two machine configurations that give rise to the same level of renewable penetration.

6.3 NPCC 48-Machine Test Case

The NPCC test case contains 140 buses and 48 synchronous machines. In PST, the models for these machines are as follows:

- Machines 1-14, 16-22 and 28-30 — two-axis machine model [16] with exciter and thermal turbine governor ($4 + 3 + 3 = 10$ states each)
- Machines 31-32, 36 — two-axis machine model (4 states each)
- Machines 15, 23-27, 33-35, 37-48 — classical machine model (2 states each)

Thus, prior to modifications, this system has 294 dynamic states.

A map with the geographical locations of each generator for the NPCC system can be found in [25]. The New England test system is a subset of the NPCC system [26]. For our reachability studies, we have retained the full machine models with associated exciter and governor models.

According to the system data provided in PST, this benchmark system has a real power generating capacity of 283.806 p.u. As in the New England test case, we perform reachability studies with the replacement of certain synchronous generators with renewable resources to achieve 10% and 20% renewable penetration.

For the reachability results presented in Figs. 6.9-6.13, several ellipsoids are obtained from various constant values of β at $t = T = 60$ s, each of which bounds the exact reach set. In the NPCC test system, we model the alternative resources as identical first-order wind farms as in (6.3).

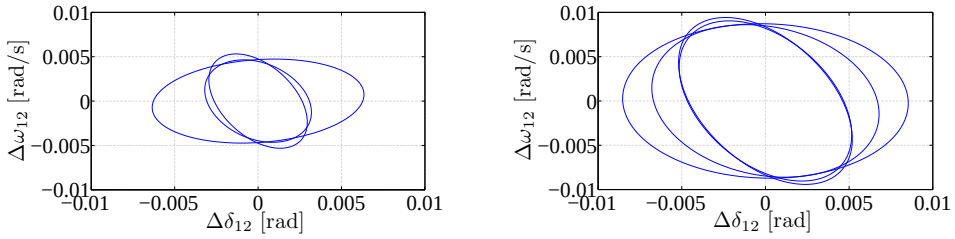

(a) ±0.3 m/s input uncertainty.

(b) ±0.6 m/s input uncertainty.

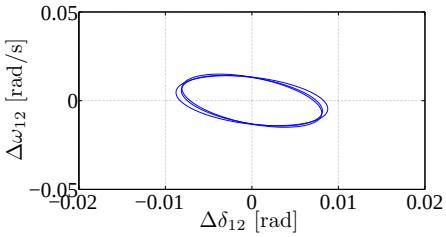

(c) ±1 m/s input uncertainty.

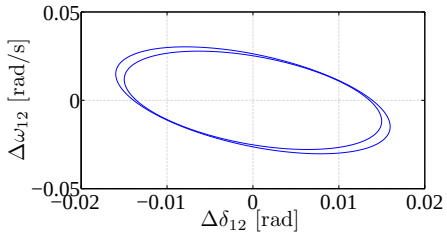

(d) ±2 m/s input uncertainty.

Figure 6.9: Reachability results for machine 12 in the NPCC test case with replacement of machines 3, 5, 6, 8, and 22, 10% renewable penetration, first-order wind farm models for the renewable resources, and unknown-but-bounded model for wind speeds.

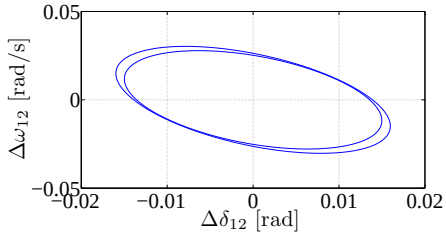

(a) Replacement of machines 3, 5, 6, 8, and 22.

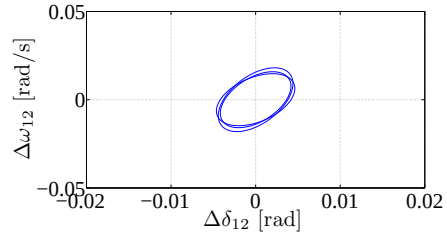

(b) Replacement of machines 31 and 44.

Figure 6.10: Reachability results for machine 12 in the NPCC test case with 10% renewable penetration, first-order wind farm models for the renewable resources, and wind speed uncertainty of ±2 m/s.

6.3.1 10% Renewable Penetration

In this section, we demonstrate the reachability results from the linearized NPCC system with 10% renewable penetration. We mimic the desired level of renewable generation by replacing

1. Machines 3, 5, 6, 8, and 22, which represent 9.97% of the system's total generation, and

2. Machines 31 and 44, which represent 10.22% of the system's total generation.

We show the reachability results for machine angle $\Delta\delta$ and speed $\Delta\omega$ of synchronous machine 12 in Figs. 6.11 and 6.10.

Fig. 6.11, again, illustrates the effect of increasing input uncertainty on the size of the reach set. The set that bounds all trajectories of the linearized system grows as the uncertainty in the wind speed forecast grows. The reachability results from two machine configurations are shown in Fig. 6.10 for wind speed uncertainty of ± 2 m/s. By inspection, we observe that even though the two cases represent approximately the same amount of renewable penetration, the variations in system variables resulting from resource uncertainty are much higher in the case where we replace machines 3, 5, 6, 8, and 22 with alternative resources. From this example, we conclude that the claim we made in Section 6.2.2 is inaccurate. Variations in system variables need not be approximately equal with a given level of renewable penetration; they may depend on machine parameters as well as network configuration (e.g., connections between synchronous machines, placement of the renewable resources, etc.).

6.3.2 20% Renewable Penetration

We illustrate the reachability results obtained from the linearized NPCC system with 20% renewable penetration. The desired level of renewable generation is mimicked by replacing

1. Machines 33, 44, 45, and 46, which represent 20.6% of the system's total generation,

2. Machines 39, 44, 45, and 46, which represent 19.8% of the system's total generation, and

3. Machines 26, 31, 33, 37, 38, 42, 43, and 45, which represent 19.0% of the system's total generation.

Reachability results for 20% renewable penetration are shown in Figs. 6.11-6.13.

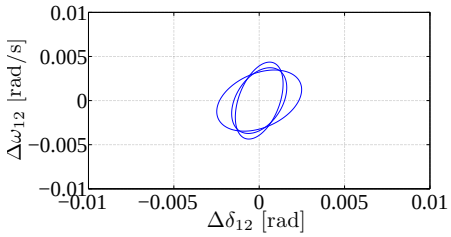

(a) ±0.3 m/s input uncertainty.

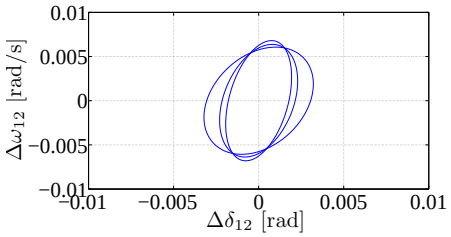

(b) ±0.6 m/s input uncertainty.

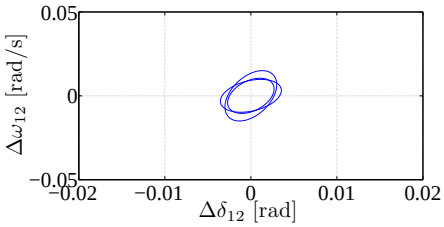

(c) ±1 m/s input uncertainty.

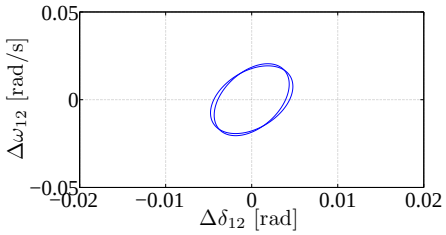

(d) ±2 m/s input uncertainty.

Figure 6.11: Reachability results for machine 12 in the NPCC test case with replacement of machines 33, 44, 45, and 46, 20% renewable penetration, first-order wind farm models for the renewable resources, and unknown-but-bounded model for wind speeds.

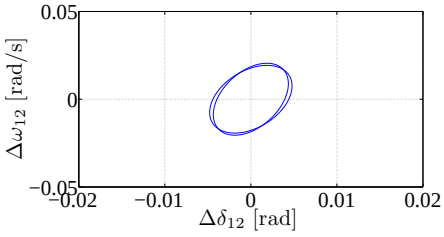

(a) Replacement of machines 33, 44, 45, and 46.

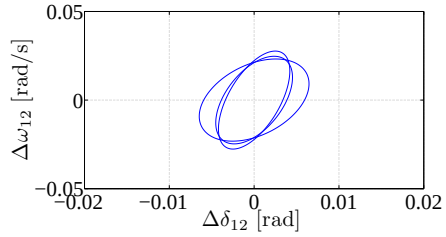

(b) Replacement of machines 39, 44, 45, and 46.

Figure 6.12: Reachability results for machine 12 in the NPCC test case with 20% renewable penetration, first-order wind farm models for the renewable resources, and wind speeds uncertainty of ±2 m/s.

In Fig. 6.11, we plot the projection of ellipsoids onto $\Delta\delta$ and $\Delta\omega$ for machine 12. Again, we observe the trend of increasing system variable variations with greater wind speed uncertainty. The displaced synchronous machines are entirely different in the approximate reach sets depicted in Fig. 6.10: machines 3, 5, 6, 8, and 22 in Fig. 6.10(b) and machines 31 and 44 in Fig. 6.10(a). In Fig. 6.12, we show reachability results from displacing a similar set of synchronous machines in the system, while maintaining about the same level

of renewable penetration. We notice that the resulting variations in system variables are approximately the same in these two cases, quite different from Fig. 6.10, even though the same system is used for the two cases. This further enforces our earlier hypothesis that variations in system variables may depend on synchronous machine parameters and the network configuration, which dictate the placement of renewable resources.

We plot the projection of bounding ellipsoids onto the subspace composed of ω_{41} and ω_8 in Fig. 6.13, resulting from the displacement of machines 26, 31, 33, 37, 38, 42, 43, and 45. We observe that the correlation between these system variables is not as great as in the New England test case.

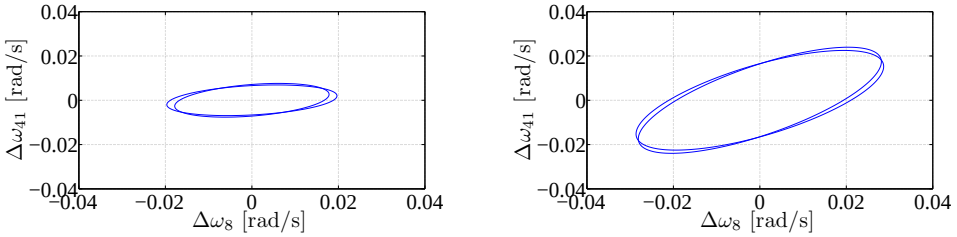

(a) ±0.6 m/s input uncertainty.

(b) ±2 m/s input uncertainty.

Figure 6.13: Reachability results for machine frequency in the NPCC test case with replacement of machines 26, 31, 33, 37, 38, 42, 43, and 45, 20% renewable penetration, and ±2 m/s wind speed uncertainty.

6.4 Summary

In this chapter, we apply the concepts presented in this thesis on three benchmark test systems: the WECC 9-bus 3-machine system, the New England 39-bus 10 machine system, and the NPCC 140-bus 48-machine system. We present two ways to visualize the reachability results:

1. Project bounding ellipsoids onto the small-signal machine angle $\Delta\delta$ and speed $\Delta\omega$ of one synchronous generator to assess individual performance,

2. Project bounding ellipsoids onto the small-signal machine speeds $\Delta\omega$ from two different synchronous generators to assess the coupled performance of two machines.

CHAPTER 7

CONCLUSIONS

This thesis proposes a method for assessing the impact of uncertain disturbances on power system dynamic performance. In particular, we focus on the impact of uncertainty in renewable-based power fluctuations. This method determines whether certain system variables deviate from prescribed values imposed by operational requirements due to uncertain input power fluctuations. We provide an analytically tractable method based on reachability analysis techniques for dynamical systems that allows us to approximate the system reach set by the reach set of the linearized system model around some nominal operating trajectory. An added advantage of our technique is its flexibility to accommodate any state-space model for the renewable resource.

The reachability concepts are demonstrated with the SMIB example where the uncontrolled input is the infinite-bus voltage. We find that our method is, indeed, sufficient to approximate the system reach set for input uncertainties of less than 15%. Then the method is applied to power systems for a three-bus configuration where a governor model is used for the classical generator. The governor model adds damping to the system and therefore we observe that the reach set remains within the WECC frequency requirements even for input renewable-based power fluctuations of ± 3 p.u.

We also apply the method to three benchmark test cases: the WECC 9-bus configuration with renewable-based generation at one bus, the New England 39-bus 10-machine system, and the NPCC 140-bus 48-machine system. The integration of renewable resources is mimicked by displacing certain synchronous generators in the system with alternative generation while maintaining the same power flow solution. The renewable resource is modelled as an unknown-but-bounded disturbance to the power system in two ways, an uncertain power injection and an uncertain weather forecast that affects the power output of a resource via a dynamic or static system. We

subject the modified system to uncertain wind speed or real power input and obtain over-approximations to the linearized system reach set. In line with the capabilities of this tool, we present several ways to visualize reachability results to obtain useful information about dynamic performance of the power system. The main conclusions from the case studies can be summarized as follows:

- The variations in system variables, such as $\Delta\delta$ and $\Delta\omega$, grow with increasing uncertainty in ΔP_i, the power injection from the i^{th} renewable resource, or Δw_i, the input variable for the i^{th} renewable resource.

- The unknown-but-bounded power input model is quite conservative, and we found that the New England system violated frequency performance requirements even for ± 0.2 p.u. uncertainty in renewable power injection. On the other hand, the input can vary greatly in the unknown-but-bounded wind speed model without violating any dynamic performance constraints. As mentioned previously, this result is expected since the unknown-but-bounded wind speed model essentially bounds the rate of change as well as the magnitude of the power injection, which is a more stringent constraint.

- Deviations of system variables away from their nominal values may be affected by, but are not limited to,

  1. levels of renewable penetration,
  2. machine characteristics, and
  3. network configurations.

- Variations in system variables are much less significant in the NPCC test system than in the New England system for the same level of renewable penetration and input uncertainty.

- The correlation between machine speeds $\Delta\omega$ is more distinct in the New England case than the NPCC system.

Our tool is applicable to the integration of renewable energy systems with existing infrastructure in order to meet our electricity demands without the economic and environmental burdens of fossil fuel consumption. We envision this tool to be used in operations, as it provides operators with a metric

of how close the system may be from violating performance requirements over a particular time window in which the power generated from renewable resources can be predicted relatively accurately. Further, we can apply our method to determine the best way to place renewable resources so as to meet dynamic performance limits. We created several scenarios in which renewable resources displaced conventional generation for the New England and NPCC test cases and subsequently obtained reachability results for each configuration. This information can be used to compare various configurations of renewable resource locations from which an optimal topology can be chosen to meet dynamic performance constraints.

The work presented in this thesis is highly applicable to power systems with small footprints, for example, in the Hawaiian islands. These systems have fewer large conventional synchronous generators and consequently less inertia. Our method to obtain approximations of the reach set enables a way to quantify renewable penetration limits in such systems so as to meet dynamic performance constraints.

Future Work

The results from this thesis can be augmented or extended in the following ways:

- Further work includes a formal analysis of the limits of the small-signal approximation to estimate the system reach set, i.e., how large can the fluctuations in the uncontrolled disturbance be so that the approximation of the true reach set by the reach set of the linearized model is valid. The SMIB results suggest that the approximation is sufficient for input deviations of less than 15%.

- The validity of our reachability results could be verified with exhaustive time-based probabilistic simulations, for example, with Monte Carlo methods, on the nonlinear system. The worst-case trajectory, obtained from time-based simulation, for the nonlinear SMIB system suggests that the reach set of the nonlinear system is contained in that of the linearized system for input fluctuations of less than 15%. It would also be beneficial to compare our ellipsoidal reachability results from the

linearized system to the outcome obtained from probabilistic methods performed on the same linearized system.

- The viability of our method could be strengthened from an analysis of the computational burden. An extension would be to quantify the scalability of this method, i.e., how much more computation would be required as the size of the system increases.

- This thesis pertains to the dynamic behaviour of the power system when subject to disturbances originating from renewable power injection. A complementary problem would be to explore reachability of power systems subject to uncertain disturbances in the context of static studies. More specifically, we could provide ellipsoidal upper bounds on bus voltages and angles based on the unknown-but-bounded power model for renewable resources.

APPENDIX A

CONTINUOUS-TIME UNKNOWN-BUT-BOUNDED PROCESS

In this appendix, we derive (3.3), reproduced as follows:

$$\frac{d}{dt}\Psi_\beta(t) = A(t)\Psi_\beta(t) + \Psi_\beta(t)A'(t) + \beta(t)\Psi_\beta(t) + \frac{1}{\beta(t)}B(t)Q(t)B'(t),$$
$$\Psi(t_0) = \Psi_0.$$

The derivation presented here borrows heavily from ideas presented in [17]. Before we begin, we present several concepts that are crucial to the derivation.

A.1 Definitions

Definition 3 (Support Function)**.** The support function, $s_{\mathcal{X}}(\eta)$, of a closed convex set $\mathcal{X}$, is defined as

$$s_{\mathcal{X}}(\eta) = \max_{x\in\mathcal{X}}\{x'\eta\}, \quad \eta'\eta = 1. \tag{A.1}$$

Then the set $\mathcal{X}$ can be expressed as

$$\mathcal{X} = \{x : x'\eta \le s(\eta)\ \forall\eta,\ \eta'\eta = 1\}. \tag{A.2}$$

◁

Definition 4 (Minkoski Sum)**.** The Minkoski sum of two closed convex sets $\mathcal{X}$ and $\mathcal{Y}$, $\mathcal{Z}$, is defined as

$$\mathcal{Z} = \{z : z = x + y, \text{for any } x \in \mathcal{X} \text{ and any } y \in \mathcal{Y}\}.$$

Let $s_{\mathcal{X}}(\eta)$, $s_{\mathcal{Y}}(\eta)$, and $s_{\mathcal{Z}}(\eta)$ denote the support functions of $\mathcal{X}$, $\mathcal{Y}$, and $\mathcal{Z}$,

respectively. Then

$$\begin{aligned} s_{\mathcal{Z}}(\eta) &= \max_{x\in\mathcal{X}, y\in\mathcal{Y}} (x+y)'\eta, \\ &= \max_{x\in\mathcal{X}} x'\eta + \max_{y\in\mathcal{Y}} y'\eta, \end{aligned}$$

so that

$$s_{\mathcal{Z}}(\eta) = s_{\mathcal{X}}(\eta) + s_{\mathcal{Y}}(\eta). \tag{A.3}$$

◁

Definition 5 (Ellipsoid)**.** The ellipsoid is a closed convex set defined as follows:

$$\mathcal{E} = \{x : [x-m]'\Gamma^{-1}[x-m] \leq 1\},$$

where Γ is a positive definite matrix. The centre of the ellipsoid is denoted by m, and the size and shape of the ellipsoid are described by Γ.

The support function for $\mathcal{E}$ is

$$s_{\mathcal{E}}(\eta) = \eta' m + \sqrt{\eta'\Gamma\eta}. \tag{A.4}$$

◁

A.2 Derivation of Ellipsoidal Equation

We begin the derivation of the ellipsoidal equation (3.3) with a model of a continuous-time unknown-but-bounded process $x(t)$ as

$$\dot{x}(t) = A(t)x(t) + B(t)w(t), \tag{A.5}$$

$$x(0) \in \mathcal{X}(0) = \{x : x'\Psi^{-1}(0)x \leq 1\}, \tag{A.6}$$

$$w(t) \in \mathcal{W}(t) = \{w : w'Q^{-1}(t)w \leq 1\}. \tag{A.7}$$

We can rewrite the continuous-time dynamics in discrete-time with $t = k\Delta$ and $\Delta \to 0$ as follows:

$$\begin{aligned} \frac{x(k\Delta+\Delta) - x(k\Delta)}{\Delta} &= A(k\Delta)x(k\Delta) + B(k\Delta)w(k\Delta), \\ x(k\Delta+\Delta) &= [I + \Delta A(k\Delta)]x(k\Delta) + \Delta B(k\Delta)w(k\Delta). \end{aligned}$$

Let $\Phi(k\Delta) = I + \Delta A(k\Delta)$ and $G(k\Delta) = \Delta B(k\Delta)$. Then the discrete-time dynamics can be written as

$$x(k\Delta + \Delta) = \Phi(k\Delta)x(k\Delta) + G(k\Delta)w(k\Delta), \tag{A.8}$$

$$x(0) \in \mathcal{X}(0) = \{x : x'\Psi^{-1}(0)x \leq 1\}, \tag{A.9}$$

$$w(k\Delta) \in \mathcal{W}(k\Delta) = \{w : w'Q^{-1}(k\Delta)w \leq 1\}. \tag{A.10}$$

Let $\mathcal{X}(k\Delta)$ denote the set containing all possible $x(k\Delta)$. $\mathcal{X}(k\Delta)$ is called the set of reachable states, or the reach set.

A.2.1 Set $k = 0$

To simplify notation, we consider, for now, the case of $k = 0$. Then (A.8) becomes

$$\begin{aligned} x(\Delta) &= \Phi(0)x(0) + G(0)w(0), \\ x(0) \in \mathcal{X}(0) &= \{x : x'\Psi^{-1}(0)x \leq 1\}, \\ w(0) \in \mathcal{W}(0) &= \{w : w'Q^{-1}(0)w \leq 1\}. \end{aligned}$$

It follows that

$$\hat{\mathcal{X}}(\Delta) = \{x : x = \Phi(0)x_1 + G(0)w, x_1 \in \mathcal{X}(0), w \in \mathcal{W}(0)\}.$$

The support function of $\mathcal{X}(0)$, an ellipsoid centered around 0, is

$$s_{\mathcal{X}(0)}(\eta) = \max_{x \in \mathcal{X}(0)} x'\eta = \sqrt{\eta'\Psi(0)\eta}.$$

Likewise, the support function of $\mathcal{W}(0)$, also an ellipsoid centered around 0, is

$$s_{\mathcal{W}(0)}(\eta) = \max_{w \in \mathcal{W}(0)} w'\eta = \sqrt{\eta'Q(0)\eta}.$$

Let $x_1 = \Phi(0)x(0)$ where $x(0) \in \mathcal{X}(0)$ and $w_1 = G(0)w(0)$ where $w(0) \in \mathcal{W}(0)$. Let $\mathcal{X}_1 = \{x_1 : x_1 = \Phi(0)x(0),\ x(0) \in \mathcal{X}(0)\}$ and $\mathcal{W}_1 = \{w_1 : w_1 =$

$G(0)w(0),\ w(0) \in \mathcal{W}(0)\}$. Then the support function of $\mathcal{X}_1$ is

$$\begin{aligned} s_{\mathcal{X}_1}(\eta) &= \max_{x \in \mathcal{X}(0)} [\Phi(0)x]'\eta = \max_{x \in \mathcal{X}(0)} x'[\Phi'(0)\eta], \\ &= \sqrt{[\Phi'(0)\eta]'\Psi(0)[\Phi'(0)\eta]}, \\ &= \sqrt{\eta'[\Phi(0)\Psi(0)\Phi'(0)]\eta}. \end{aligned}$$

Similarly, the support function of $\mathcal{W}_1$ is

$$s_{\mathcal{W}_1}(\eta) = \sqrt{\eta'[G(0)Q(0)G'(0)]\eta}.$$

Clearly $\hat{\mathcal{X}}(\Delta)$ is the Minkoski sum of $\mathcal{X}_1$ and $\mathcal{W}_1$. Thus, using (A.3), the support function of $\mathcal{X}(\Delta)$ is

$$\begin{aligned} s_{\hat{\mathcal{X}}(\Delta)} &= s_{\mathcal{X}_1} + s_{\mathcal{W}_1} \\ &= \sqrt{\eta'[\Phi(0)\Psi(0)\Phi'(0)]\eta} + \sqrt{\eta'[G(0)Q(0)G'(0)]\eta}. \end{aligned} \tag{A.11}$$

In general, (A.11) is not the support function of an ellipsoid. However, we can make use of the special case of Holder's inequality [1] to find the support function of a bounding ellipsoid $\mathcal{X}(\Delta)$ as follows:

$$s_{\hat{\mathcal{X}}(\Delta)} \leq \left\{ \eta' \underbrace{\left[\frac{1}{1-\gamma}\Phi(0)\Psi(0)\Phi'(0) + \frac{1}{\gamma}G(0)Q(0)G'(0) \right]}_{\Psi(\Delta)} \eta \right\}^{1/2}, \quad 0 < \gamma < 1.$$

Thus, $\hat{\mathcal{X}}(\Delta) \subset \mathcal{X}(\Delta) = \{x : x'\Psi^{-1}(\Delta)x \leq 1\}$.

We can apply the development in Section A.2.1 to each time step, i.e., for every value of k to obtain the general relation

$$\begin{aligned} \Psi(k\Delta + \Delta) = &\frac{1}{1-\gamma}\Phi(k\Delta)\Psi(k\Delta)\Phi'(k\Delta) \\ &+ \frac{1}{\gamma}G(k\Delta)Q(k\Delta)G'(k\Delta), \quad 0 < \gamma < 1. \end{aligned} \tag{A.12}$$

with $\hat{\mathcal{X}}(k\Delta + \Delta) \subseteq \mathcal{X}(k\Delta + \Delta) = \{x : x'\Psi^{-1}(k\Delta + \Delta)x \leq 1\}$.

[1] $(b_1 + b_2)^2 \leq (1-\gamma)^{-1}b_1^2 + \gamma^{-1}b_2^2, \quad 0 < \gamma < 1.$

Let $\gamma = \Delta\beta$. Then (A.12) becomes

$$\Psi(k\Delta+\Delta) = \frac{1}{1-\Delta\beta}\Phi(k\Delta)\Psi(k\Delta)\Phi'(k\Delta) + \frac{1}{\Delta\beta}G(k\Delta)Q(k\Delta)G'(k\Delta), \quad 0<\beta<\infty. \tag{A.13}$$

Since $\Delta\beta << 1$, we approximate $\frac{1}{1-\Delta\beta}$ as $1+\Delta\beta$. Thus, (A.13) becomes

$$\begin{aligned}\Psi(k\Delta+\Delta) &\approx (1+\Delta\beta)\Phi(k\Delta)\Psi(k\Delta)\Phi'(k\Delta) + \frac{1}{\Delta\beta}G(k\Delta)Q(k\Delta)G'(k\Delta)\\ &= (1+\Delta\beta)[I+\Delta A(k\Delta)]\Psi(k\Delta)[I+\Delta A(k\Delta)]' + \frac{1}{\Delta\beta}[\Delta B(k\Delta)]Q(k\Delta)[\Delta B'(k\Delta)].\end{aligned} \tag{A.14}$$

Since Δ is small, we can neglect the higher ordered terms in Δ from (A.14) and continue as follows:

$$\Psi(k\Delta+\Delta) \approx \Psi(k\Delta) + \Delta A(k\Delta)\Psi(k\Delta) + \Delta\Psi(k\Delta)A'(k\Delta) + \Delta\beta\Psi(k\Delta) + \frac{\Delta}{\beta}B(k\Delta)Q(k\Delta)B'(k\Delta).$$

Rearranging, we obtain

$$\frac{\Psi(k\Delta+\Delta)-\Psi(k\Delta)}{\Delta} \approx A(k\Delta)\Psi(k\Delta) + \Psi(k\Delta)A'(k\Delta) + \beta\Psi(k\Delta) + \frac{1}{\beta}B(k\Delta)Q(k\Delta)B'(k\Delta). \tag{A.15}$$

Recognizing that (A.15) is the discrete-time approximation of a continuous-time differential equation, we obtain (3.3)

$$\frac{d}{dt}\Psi(t) = A(t)\Psi(t) + \Psi(t)A'(t) + \beta\Psi(t) + \frac{1}{\beta}B(t)Q(t)B'(t),$$
$$\Psi(0) = \Psi_0.$$

APPENDIX B

PROJECTIONS OF SETS

Consider some K-dimensional closed, convex set $\mathcal{X}$ where

$$\mathcal{X} = \{x : g(x) \leq 0\}, \tag{B.1}$$

where $x = [x_1' \quad x_2']'$, x_1 and x_2 are K_1 and K_2-dimensional vectors, respectively. Let $\mathcal{X}_1$ denote the projection of $\mathcal{X}$ onto the K_1-dimensional subspace of x_1. Then

$$\mathcal{X}_1 = \{x_1 : g(x_1, x_2) \leq 0, \text{for any } x_2\}. \tag{B.2}$$

The projection can be obtained as the result of the following special linear transformation:

$$x_1 = Hx, \tag{B.3}$$

where $H = [I \quad 0]$ and x_1 is a K_1-dimensional vector.

APPENDIX C

MATLAB IMPLEMENTATION DETAILS

The reachability problem described in this thesis is solved in MATLAB in conjunction with Power System Toolbox (PST), the functionalities of which are outlined in [27].

C.1 System Matrices from PST

The function svm_mgen.m is run on the test system to obtain three relevant matrices: a_mat, b_pm, and mac_state. These matrices create the following small-signal model:

$$\Delta\dot{x} = [\text{a\_mat}]\Delta x + [\text{b\_pm}]\Delta P_m,$$

where Δx denotes the small-signal dynamic states and ΔP_m denotes the vector of small-signal mechanical power input into each synchronous machine.

The matrix mac_state contains three columns and as many rows as system states. Each row corresponds to a state. The first column contains the sequential numbering for the states; the second denotes the name of the states, for example, 1 corresponds to the machine angle δ and 2 corresponds to the machine frequency ω; and finally the third column describes the machine with which that state is associated.

We utilize data for test cases that are packaged with PST. To mimic the penetration of renewable resources, we replace several synchronous machines with renewable power generation by modifying the test case data in two ways. First, we reduce the order of the synchronous machine model to the classical model with only two dynamic states, the machine angle (δ) and speed (ω). Second, we modify the data for these machines to have unrealistically fast dynamics, appropriate for applying the singular perturbation model later. In particular, we reduce the machine inertia, denoted by H, and increase the

machine damping, to create unrealistically large eigenvalues, corresponding to very fast dynamics.

C.2 Conversion from Per-Unit Speed

PST generates its matrices based on per-unit speeds (ω) as in [28]. The relationship used to convert from per-unit speed is $\Delta\omega_r = \omega_s \Delta\bar{\omega}_r$, where $\Delta\bar{\omega}_r$ denotes the per-unit variable, ω_s is the synchronous frequency $2\pi 60$, and $\Delta\omega_r$ denotes the non per-unit variable. Consequently,

$$\frac{d\Delta\omega_r}{dt} = \omega_s \frac{d\Delta\bar{\omega}_r}{dt}.$$

To convert back from per-unit frequencies, we multiply the $\Delta\omega$ rows by ω_s in both a_mat and b_pm matrices and divide the columns that multiply $\Delta\omega$ by ω_s in a_mat. We check the correctness of this step by ensuring the eigenvalues do not change after the operations have been performed.

C.3 Removal of Zero-Eigenvalue Associated with Reference Angle

In any rotational system, the reference for angles is arbitrary. Thus, a zero-eigenvalue is always present in the system. Due to the numerical nature in which PST performs linearization, however, the a_mat matrices almost always contain a very small positive eigenvalue. This makes the matrix unstable, which is not the correct inference since these power systems are stable in reality.

To remove the zero-eigenvalue, we select δ_1, the angle on machine 1, as the reference, and subsequently apply the following coordinate transformation [16]:

$$\begin{aligned}
\delta_i' &= \delta_i - \delta_1, \quad i = 2, \ldots, m, \\
\delta_i' &= 0, \\
\dot{\delta}_i' &= \omega_i - \omega_1, \quad i = 2, \ldots, m, \\
\dot{\delta}_1' &= 0,
\end{aligned}$$

where m denotes the number of machines present in the system. This implies the differential equation corresponding to $\Delta\delta_1$ can be deleted. Also, the column corresponding to $\Delta\delta_1$ is deleted. The differential equations $\Delta\dot{\delta}_i = \Delta\omega_i$, $i = 2, \ldots, m$, are replaced by $\Delta\dot{\delta}_i = \Delta\omega_i - \Delta\omega_1$. In the a_mat matrix, we place -1 in the intersections of the rows corresponding to $\Delta\dot{\delta}_i$ and the column corresponding to $\Delta\omega_1$. We check the result of this step by ensuring the slightly positive eigenvalue no longer exists.

C.4 Application of Singular Perturbation Model

The singular perturbation model [19] is

$$\begin{aligned} \dot{x} &= f(t, x, z, \epsilon), \\ \epsilon\dot{z} &= g(t, x, z, \epsilon), \end{aligned}$$

where ϵ is small.

In our test system, we prepare unrealistically fast dynamics for synchronous machines that have been replaced by renewable generation. For these 'fast' machines, we obtain differential equations of the form,

$$\begin{aligned} \Delta\dot{\delta}_p &= \Delta\omega_p - \Delta\omega_1, \\ \frac{2H_p}{\omega_s}\Delta\dot{\omega}_p &= \ldots, \end{aligned}$$

where $2H_p/\omega_s$ is small and p denotes machines to be singularly perturbed. The problem that arises is that both $\Delta\delta_p$ and $\Delta\omega_p$ are fast dynamics, but the small constant ϵ does not appear in front of both differential equations. To solve this, we substitute

$$\Delta\omega'_p = \sqrt{\frac{2H_p}{\omega_s}}\Delta\omega_p \quad \text{and} \quad \Delta\omega'_1 = \sqrt{\frac{2H_p}{\omega_s}}\Delta\omega_1.$$

Consequently,

$$\Delta\dot{\omega}'_p = \sqrt{\frac{2H_p}{\omega_s}}\Delta\dot{\omega}_p \quad \text{and} \quad \Delta\dot{\omega}'_1 = \sqrt{\frac{2H_p}{\omega_s}}\Delta\dot{\omega}_1.$$

This implies we can divide the columns corresponding to $\Delta\omega_p$ and $\Delta\omega_1$ by

$\sqrt{2H_p/\omega_s}$, and multiply the differential equations corresponding to $\Delta\omega_p$ by $\sqrt{2H_p/\omega_s}$. To correctly apply the singular perturbation model with the same small time constant ϵ, we must ensure H_p is chosen to be the same value for all the synchronous machines that we replace as renewable generation.

The resulting equations for these 'fast' machines are

$$\sqrt{\frac{2H_p}{\omega_s}}\Delta\dot{\delta}_p = \Delta\omega_p' - \Delta\omega_1',$$
$$\sqrt{\frac{2H_p}{\omega_s}}\Delta\dot{\omega}_p' = \dots.$$

Singular perturbation is then easily applied as follows:

$$\begin{bmatrix} \Delta\dot{x}_n \\ \sqrt{\frac{2H_p}{\omega_s}}\Delta\dot{x}_p \end{bmatrix} = \begin{bmatrix} A_{11} & A_{12} \\ A_{21} & A_{22} \end{bmatrix} \begin{bmatrix} \Delta x_n \\ \Delta x_p \end{bmatrix} + \begin{bmatrix} B_1 \\ B_2 \end{bmatrix} \Delta u.$$

By approximating $\sqrt{\frac{2H_p}{\omega_s}}$ as 0, i.e., Δx_p can change instantaneously, we obtain

$$\begin{bmatrix} \Delta\dot{x}_n \\ 0 \end{bmatrix} = \begin{bmatrix} A_{11} & A_{12} \\ A_{21} & A_{22} \end{bmatrix} \begin{bmatrix} \Delta x_n \\ \Delta x_p \end{bmatrix} + \begin{bmatrix} B_1 \\ B_2 \end{bmatrix} \Delta u,$$

from which we obtain $\Delta x_p = -A_{22}^{-1}[A_{21}\Delta x_n + B_2\Delta u]$, and

$$\begin{aligned} \Delta\dot{x}_n &= A_{11}\Delta x_n + A_{12}\Delta x_p + B_1\Delta u, \\ \Delta\dot{x}_n &= A_{11}\Delta x_n - A_{12}A_{22}^{-1}\left[A_{21}\Delta x_n + B_2\Delta u\right] + B_1\Delta u, \\ \Delta\dot{x}_n &= \underbrace{\left[A_{11} - A_{12}A_{22}^{-1}A_{21}\right]}_{\tilde{A}}\Delta x_n + \underbrace{\left[B_1 - A_{12}A_{22}^{-1}B_2\right]}_{\tilde{B}}\Delta u. \end{aligned}$$

C.5 Augmentation of Renewable Resource Dynamics

As described in Chapter 4, we augment the power systems dynamics with those of the renewable resource as follows:

$$\begin{bmatrix} \Delta\dot{x}_n \\ \Delta\dot{\xi} \end{bmatrix} = \underbrace{\begin{bmatrix} \tilde{A} & 0 \\ 0 & F \end{bmatrix}}_{\bar{A}} \begin{bmatrix} \Delta x \\ \Delta\xi \end{bmatrix} + \underbrace{\begin{bmatrix} \tilde{B} & 0 \\ 0 & G \end{bmatrix}}_{\bar{B}} \begin{bmatrix} \Delta u \\ \Delta w \end{bmatrix},$$

where $\Delta\xi$ denotes the augmented states and Δw represents the inputs to the renewable resource processes.

C.6 Solution of Reachability Problem

Finally, we solve the reachability problem with uncertainty in $\Delta w \in \Delta\mathcal{X}_{\Delta w}$ using (3.3) with $\bar{A}$ and $\bar{B}$.

REFERENCES

[1] P. Eriksen, T. Ackermann, H. Abildgaard, P. Smith, W. Winter, and J. R. Garcia, "System operation with high wind penetration," *IEEE Power and Energy Magazine*, vol. 3, no. 6, pp. 65–74, Nov.-Dec. 2005.

[2] Z. Dong and P. Zhang, *Emerging Techniques in Power System Analysis*. Springer-Verlag, 2010.

[3] M. Bartels, C. Gatzen, M. Peek, W. Schulz, R. Wissen, A. Jansen, J. P. Molly, B. Neddermann, H.-P. Gerch, E. Grebe, Y. Sanick, and W. Winter, "Planning of the grid integration of wind energy in Germany onshore and offshore up to the year 2020," *International Journal of Global Energy Issues*, vol. 25, no. 3-4, pp. 257–275, 2006.

[4] D. Gautam, V. Vittal, and T. Harbour, "Impact of increased penetration of dfig-based wind turbine generators on transient and small signal stability of power systems," *IEEE Transactions on Power Systems*, vol. 24, no. 3, pp. 1426–1434, Aug. 2009.

[5] P. Kundur, J. Paserba, V. Ajjarapu, G. Andersson, A. Bose, C. Canizares, N. Hatziargyriou, D. Hill, A. Stankovic, C. Taylor, T. Van Cutsem, and V. Vittal, "Definition and classification of power system stability," *IEEE Transactions on Power Systems*, vol. 19, no. 2, pp. 1387–1401, May 2004.

[6] F. Alvarado, Y. Hu, and R. Adapa, "Uncertainty in power system modeling and computation," in *Proc. of the IEEE International Conference on Systems, Man and Cybernetics*, Oct. 1992.

[7] Z. Wang and F. Alvarado, "Interval arithmetic in power flow analysis," *IEEE Transactions on Power Systems*, vol. 7, no. 3, pp. 1341–1349, Aug. 1992.

[8] A. Saric and A. Stankovic, "Model uncertainty in security assessment of power systems," *IEEE Transactions on Power Systems*, vol. 20, no. 3, pp. 1398–1407, Aug. 2005.

[9] A. Saric and A. Stankovic, "An application of interval analysis and optimization to electric energy markets," *IEEE Transactions on Power Systems*, vol. 21, no. 2, pp. 515 – 523, May 2006.

[10] A. Saric and A. Stankovic, "Applications of ellipsoidal approximations to polyhedral sets in power system optimization," *IEEE Transactions on Power Systems*, vol. 23, no. 3, pp. 956–965, Aug. 2008.

[11] J. Hockenberry and B. Lesieutre, "Evaluation of uncertainty in dynamic simulations of power system models: The probabilistic collocation method," *IEEE Transactions on Power Systems*, vol. 19, no. 3, pp. 1483–1491, Aug. 2004.

[12] I. Hiskens and J. Alseddiqui, "Sensitivity, approximation, and uncertainty in power system dynamic simulation," *IEEE Transactions on Power Systems*, vol. 21, no. 4, pp. 1808 –1820, Nov. 2006.

[13] I. Hiskens and M. Pai, "Trajectory sensitivity analysis of hybrid systems," *IEEE Transactions on Circuits and Systems I: Fundamental Theory and Applications*, vol. 47, no. 2, pp. 204 –220, Feb. 2000.

[14] L. Jin, R. Kumar, and N. Elia, "Reachability analysis based transient stability design in power systems," *International Journal of Electrical Power and Energy Systems*, vol. 32, no. 7, pp. 782–787, 2010.

[15] H. A. Pulgar-Painemal, "Wind farm model for power system stability analysis," Ph.D. dissertation, University of Illinois at Urbana-Champaign, 2010.

[16] P. Sauer and M. Pai, *Power System Dynamics and Stability*. Upper Saddle River, NJ: Prentice-Hall, Inc., 1998.

[17] F. Schweppe, *Uncertain Dynamic Systems*. Englewood Cliffs, NJ: Prentice-Hall Inc., 1973.

[18] F. Chernousko, "Ellipsoidal state estimation for dynamical systems," *Nonlinear Analysis*, vol. 63, no. 5-7, pp. 872–879, 2005.

[19] H. Khalil, *Nonlinear Systems*. Upper Saddle River, NJ: Prentice-Hall, Inc., 2002.

[20] D. Angeli and E. Sontag, "Forward completeness, unboundedness observability, and their Lyapunov characterizations," *Systems Control Letters*, vol. 38, no. 4-5, pp. 209–217, 1999.

[21] A. Kurzhanski and P. Varaiya, "Ellipsoidal techniques for reachability analysis. Parts I & II," *Optimization Methods and Software*, vol. 17, pp. 177–237, Feb. 2002.

[22] F. Chernousko and A. Ovseevich, "Properties of the optimal ellipsoids approximating the reachable sets of uncertain systems," *Journal of Optimization Theory and Applications*, vol. 120, no. 2, pp. 223–246, Feb. 2004.

[23] R. Horn and C. Johnson, *Topics in Matrix Analysis*. New York, NY: Cambridge University Press, 1991.

[24] Western Electricity Coordinating Council (WECC), "WECC coordinated off-nominal frequency load shedding and restoration requirements," July 2005. [Online]. Available: http://www.wecc.biz/library/default.aspx

[25] J. Chow, R. Galarza, P. Accari, and W. Price, "Inertial and slow coherency aggregation algorithms for power system dynamic model reduction," *IEEE Transactions on Power Systems*, vol. 10, no. 2, pp. 680 –685, May 1995.

[26] R. Galarza, J. Chow, W. Price, A. Hargrave, and P. Hirsch, "Aggregation of exciter models for constructing power system dynamic equivalents," *IEEE Transactions on Power Systems*, vol. 13, no. 3, pp. 782 –788, Aug. 1998.

[27] J. Chow and K. Cheung, "A toolbox for power system dynamics and control engineering education and research," *IEEE Transactions on Power Systems*, vol. 7, no. 4, pp. 1559 –1564, Nov. 1992.

[28] P. Kundur, *Power System Stability and Control*. New York, NY: McGraw-Hill, Inc., 1993.